Tectonophysics 752 (2019) 1–23

Contents lists available at ScienceDirect

Tectonophysics

journal homepage: www.elsevier.com/locate/tecto

Present-day kinematic behaviour of active faults in the Eastern Alps

Ivo Baroň[a,b,*], Lukas Plan[a], Luboš Sokol[c], Bernhard Grasemann[d], Rostislav Melichar[c], Ivanka Mitrovic[a,d], Josef Stemberk[b]

[a] Cave and Karst Research Group, Dep. of Geology and Paleontology, Natural History Museum, Burgring 7, 1010 Vienna, Austria
[b] Institute of Rock Structure and Mechanics, The Czech Academy of Sciences, V Holešovičkách 94/41, 182 09 Prague, Czech Republic
[c] Department of Geological Sciences, Faculty of Science, Masaryk University, Kotlářská 2, Brno, Czech Republic
[d] Department of Geodynamics and Sedimentology, University of Vienna, Althanstraße 14, 1090 Vienna, Austria

ARTICLE INFO

Keywords:
Active fault
Kinematics
Fault displacement
Monitoring
Eastern Alps

ABSTRACT

The Neogene to Quaternary lateral extrusion of the Eastern Alps towards the Pannonian Basin is accommodated by a system of strike-slip faults. Despite decades-lasting GPS observations, no information on contemporary kinematic behaviour of these faults has been available. Therefore, we had monitored subsidiary and/or conjugated faults associated to these major fault systems in six caves throughout the Eastern Alps over a 1.5–2.5-year observation period by means of high-resolution three-dimensional Moiré extensometers TM71. We confirmed that the monitored faults revealed present-day aseismic displacements at a micrometer level during several activity phases that usually also coincided with periods of increased local seismicity. The annual displacement rates of the monitored faults were mostly about an order of magnitude smaller than the rates of the entire crustal wedges revealed from GNSS. The particular displacements consisted of a variety mechanisms and faulting regimes. Fault dilations and compressions were mostly associated with thermal-volumetric variations, normal dip-slips and downward hanging-wall displacements originated due to gravitational relaxation or mass movement. Displacements with the same mechanisms as the geologically documented fault systems or with an upward component were attributed to tectonic creep and strain built-up during the interseismic period. On the other hand, the countervailing displacements opposite to the master fault kinematics were most probably caused by elastic rebound. They were usually registered few days in advance to distinct local earthquakes that were simultaneously activated at locked segments within the same deformation band. Therefore, the countervailing events could be considered an indicator of impending near earthquake within the rebound zone; their better understanding and real-time detecting could be a step forward to an effective earthquake early warning in similar geological settings.

1. Introduction

Observing recent tectonic activity is currently an attractive topic of several geodynamic studies worldwide (e.g., Agnew, 2007; Cello and Kostak, 2003; Georgieva et al., 2016; He et al., 2010; Košťák et al., 2011; Parcharidis et al., 2009), but it is usually restricted to geological/geomorphic documentation of the past fault reactivations (McCalpin, 1996), indirect seismological methods (Isacs and Molnar, 1971; Hardebeck and Michael, 2006; Roux and Ben-Zion, 2013), uni- and multi-component strainmeters and tiltmeters (Ishii et al., 2002), and remotely-sensed measuring the horizontal movement components of regional ground-surface deformation by Global Navigation Satellite Systems (GNSS) or the vertical component of the ground deformation by satellite radar interferometry (e.g., Elliott et al., 2016; Pinel-Puysségur et al., 2014; Tamburini et al., 2014). All these approaches, however, cannot fully describe the character and nature of particular fault kinematic behavior in 3D. This may only be done using three dimensional extensometers with micrometric resolution to fully characterize the kinematic behaviour of the respective fault blocks over a longer interseismic period (e.g., Košťák and Avramova-Tačeva, 1988; Košťák et al., 1992; Stemberk et al., 2003; Šebela et al., 2010; Briestenský et al., 2015, 2018; Rinaldi-Montes et al., 2017; Blahůt et al., 2018; Sokol et al., 2018). This could be important especially for the fault behavior during an interseismic cycle, when displacements along faults are very small. The broadest network of such three dimensional and high resolutional extensometers is operated in the framework of the EU-TecNet to record transient deformations across individual faults worldwide (Briestenský et al., 2015). In our study, we adopted the

* Corresponding author at: Institute of Rock Structure and Mechanics, The Czech Academy of Sciences, V Holešovičkách 94/41, 182 09 Prague, Czech Republic
E-mail address: baron@irsm.cas.cz (I. Baroň).

https://doi.org/10.1016/j.tecto.2018.12.024
Received 30 May 2018; Received in revised form 18 December 2018; Accepted 24 December 2018
Available online 06 January 2019

approach of the EU-Tecnet to the Eastern Alps, where up-to-date knowledge of present-day fault kinematics had completely been missing.

The modern complex structure of the Eastern Alps results from a convergence between the Adriatic and the European Plates (e.g., Frisch, 1979; Neubauer et al., 2000; Schmid et al., 2004; Brückl et al., 2010; Handy et al., 2015). The continent-continent collision started after subduction and thrusting of the Penninic flysch units during the Eocene about 50 Ma ago (Decker and Peresson, 1996). The indentation of the rigid South Alpine indenter and north-south shortening of the collision zone between the Adriatic Plate and the Bohemian Massif of the European Plate was followed by post-collisional shortening of the collision zone until the Miocene, when the major component of the deformation switched from north-south shortening to west-east orogen parallel extension (Decker and Peresson, 1996).

This orogen-parallel extension is closely linked to crustal thickening and exhumation of the Tauern Window and has been accommodated by low angle normal faults and systems of strike-slip faults. The low-angle normal faults occur, e.g. at the eastern and western margin of the Tauern Window (Fügenschuh et al., 1997). The system of strike-slip faults is represented by the sinistral WSW to SW-trending faults along the northern margin and the dextral WNW to NW-striking faults along the southern margin of the eastward extruding crustal blocks (Ratschbacher et al., 1991). The most prominent sinistral fault systems include the Salzach-Ennstal-Mariazell-Puchberg Fault System (SEMP), Mur-Mürz Fault System (MM), Vienna Basin Transfer Fault (VBT) and several other less prominent faults within the Northern Calcareous Alps (Peresson and Decker, 1997). On the other hand, the dextral faults include, e.g., the Periadriatic Line (PAL), and Pöls-Lavanttal (LA) fault systems to the south of the crustal blocks (Fig. 1).

Seismic activity and geodetically observed displacements show that major tectonic activity due to continuing convergence between Africa and Europe has shifted southward to the subduction zones in the Mediterranean (Brückl et al., 2010). However, the tectonic processes in the Eastern Alps started in the Miocene and are still active but diminishing (e.g., Reinecker and Lenhardt, 1999; Decker et al., 2005; Grenerczy and Kenyeres, 2006). The seismic hazard is estimated to be moderate (Stein et al., 2015). The lateral extrusion of crustal blocks of the Eastern Alps towards the Pannonian Basin is considered one of the main recent tectonic processes in the Alpine-Carpathian-Pannonian region (Ratschbacher et al., 1991; Wölfler et al., 2011).

Data on the activity of the strike-slip fault systems have mainly been obtained by geological survey or derivation from the geophysical data. The first radiometrically proved geological evidence of a recently active tectonic fault in the Eastern Alps was presented by Plan et al. (2010) from a branch of the SEMP fault exposed in Hirschgruben Cave in the Northern Calcareous Alps that reactivated between 11 and 86 ka in the Late Pleistocene. Recently, in the Northern Calcareous Alps there was also identified a Quaternary co-seismic soft sediment deformation in Hirlatz Cave near Hallstatt (Salomon et al., 2018). In the Vienna Basin east of the Alps, Beidinger et al. (2011), Weissl et al. (2017) and Hintersberger et al. (2018) identified several past earthquakes using paleoseismological and archaeological approaches.

Decades-lasting Global Navigating Satellite Systems (GNSS) observations of the ground-surface deformation in the Eastern Alps (Grenerczy, 2005; Bus et al., 2009; Serpelloni et al., 2016) confirmed the active escape of crustal blocks east of the Tauern Window towards the Pannonian Basin at a velocity of about 1.4 ± 0.2 mm/year. Despite

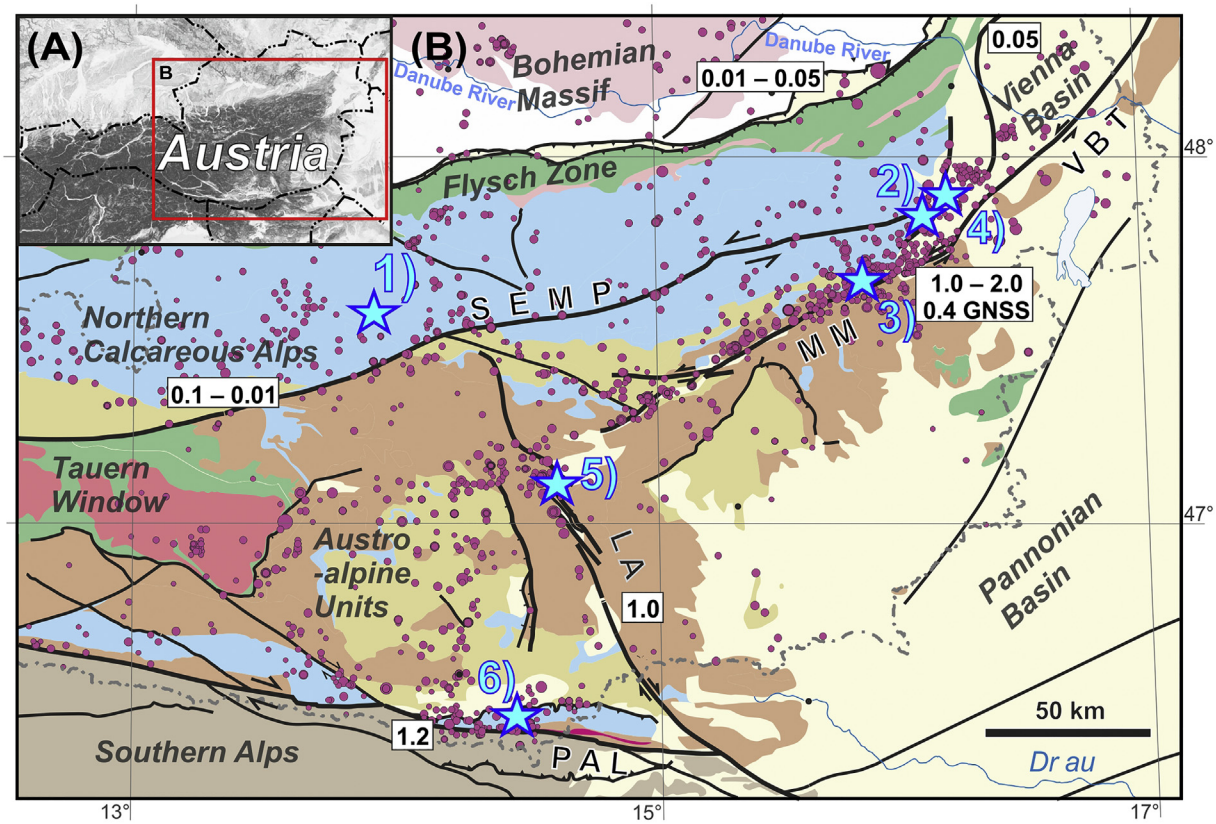

Fig. 1. General settings of the study area: (A) slope map of Austria and the Eastern Alps with depicted detailed Fig. 1 B, (B) tectonic overview map of the eastern part of the Eastern Alps (modified after Schuster et al., 2014) with presented major tectonic faults and their approximate annual displacement rates in mm/yr (white boxes), earthquake epicentres, and the study sites, i.e.: 1 – Bullen Cave, 2 – Emmerberg Cave, 3 – Zederhaus Cave, 4 – Eisenstein Cave, 5 – Geierkogel Cave, and 6 – Obir Cave, SEMP – Salzach-Ennstal-Mariazell-Puchberg fault system, MM – Mur-Mürz fault system, VBT – Vienna Basin Transfer fault, LA – Pöls-Lavanttal fault system, PAL – Periadriatic Line fault system. Source of data: SRTM USGS/NASA and ZAMG; fault displacement rates after Basili et al. (2013) and Vrabec et al. (2006), GNSS value for MM after Umnig and Weber (2017).

these indirect observations, no direct measurements of the contemporary fault kinematic behaviour exist in the Eastern Alps. Based on these first geological and geophysical observations of active tectonics in the Eastern Alps, the major goal of this study was direct measurement of possible active fault movement within the seismic cycle.

2. Methods

We built up a monitoring network at six sites in the Eastern Alps consisting of micrometer-resolution three-dimensional extensometers TM71 (Baroň et al., 2016). The instruments were installed in karst caves where active faults were well indicated by the offset of solutional cave walls. We focused on tectonically active areas along major fault systems, where relatively high seismic activity had been recorded. In the first step, we analysed geological maps together with the ground surface shape in order to identify the geomorphological signal of potential active faults using 1 m-resolution digital terrain models (DTM). These DTMs were derived from airborne laser scanning (ALS). The areas of potential interest were then compared to the Austrian cave register that is available online as a GIS database (Spelix, n.d). Caves in close vicinity of faults were inspected in order to identify potential markers of recent fault activity. We focused on tectonically deformed flowstones, recent rock crushing or off-setting solutional cave surfaces. At sites with possible tectonic fault activity in accordance to the regional active-tectonic pattern, automated 3D opto-mechanical extensometers TM71 were installed (Košťák, 1991; Klimeš et al., 2012). These devices were connected to respective fault blocks by massive iron tubes.

The measuring principle of TM71 is based on the mechanical interference between two glass indicators with optical grids causing Moiré patterns, which were described in detail by Košťák and Popp (1966) and Rowberry et al. (2016). The Moiré patterns are registered by Web-cameras connected to field computers and need to be transformed into metric values either manually (Košťák and Popp, 1966) or automatically (Marti et al., 2013). The centre-to-centre distance between the glass plates is calculated using the number of fringes and the direction of the displacement indicated by the principal axis of the symmetry pattern (e.g. Rowberry et al., 2016). When considering the number of fringes, the instrumental resolution is 25 μm but this can be improved up to 1 μm resolution by measuring rotations of the principal axis.

The TM71 devices were complemented with automatic meteorological stations recording air temperature, air pressure, and air humidity at the devices. The measurements were recorded on a daily basis at 00:00 a.m. UTC. Later in course of the project, hourly readings were taken at four sites with a permanent power supply. The environment in the caves is well shielded from external factors, especially from external diurnal thermal fluctuations and thermal-volumetric changes of rock and of the extensometer (Gosar et al., 2009; Briestenský et al., 2010).

Outputs of the TM71 device are the x, y and z components of the relative displacement of the blocks, where positive x refers to compression in the direction of internal axis, positive y refers to horizontal sinistral movement, positive z refers to vertical movement and gxy and gxz are rotations in horizontal and vertical XZ planes. The results are commonly presented as particular movement components of the cumulative displacements (e.g., Briestenský et al., 2010, 2015; Stemberk and Košťák, 2007; Stemberk et al., 2017), or as the displacement vector of the hanging block.

The magnitude and geographic orientation of the hanging block displacement vectors were calculated from the orthogonal components measured by TM71 in three steps:

(i) converting the x, y, z components to vector of displacement of the hanging wall $\mathbf{P} = [P_x, P_y, P_z]^T$ in the geographic coordinate system, where positive P_x was the north-directed horizontal displacement of hanging wall, positive P_y was east-directed horizontal displacement of hanging wall and positive P_z was down-directed vertical displacement of hanging wall;
(ii) the vector **P** was then normalized to a unit vector $\mathbf{P'} = [P'_x, P'_y, P'_z]^T$ with the same direction as **P** but with length equal 1;
(iii) the trend (α_L) and plunge (Φ_L) of the hanging wall displacement P was then calculated according to following equations:

$$\alpha_L = \arctan (P'_y/P'_x)$$

$$\Phi_L = \arcsin P'_z$$

Then, the displacement vectors were plotted in the lower hemisphere stereographic projection. Based on the displacement magnitudes we calculated a *total sum of all individual displacement events* (*Ds*) that is a sum of the absolute values of each particular displacement vector irrespective to nature or orientation. In contrary, the *cumulative displacement magnitude* (*Dc*) and its orientation were calculated from the sum of each particular movement component x, y, z of TM71 device for the whole period of observation separately. Using this cumulative displacement for a period covering at least one full year we could eliminate the periodic and reversible trends (e.g., attributed to the climatic cycle). The ratio called *Index of Periodicity* ($Ip = Dc/Ds$) then indicated the prevailing periodic versus irreversible nature of the displacements within the period of observation; the displacements lack a periodic component when $Ip = 1$.

3. Geological and tectonic setting

This study focuses on the major fault systems in the Eastern Alps described in the following section. An overview of the monitored active faults is presented in Table 1.

3.1. Salzach-Ennstal-Mariazell-Puchberg (SEMP) fault system

The sinistral SEMP Fault System is oriented WSW-ENE and reaches a total length of about 400 km from the Tauern Window in the West to the Vienna Basin in the East (Fig. 1). The total sinistral offset reaches up to about 70 km and the observed deformation has a ductile character in the western section, the ductile-brittle one in the central section and completely brittle to the East (Linzer et al., 2002). The originally relatively straight and narrow fault splays into several branches towards the East (Linzer et al., 2002). Basili et al. (2013) estimated a 0.1 to 0.01 mm/yr displacement rate for the western and central sections of the SEMP fault system.

One monitoring site was set up near the central segment of SEMP fault system, another at its termination near the Vienna Basin to the

Table 1
Overview of monitored sites and faults.

Location	Fault systém	Monitored fault orientation dip direction/dip angle [°]	Fault kinematics	Macroscopic offset [mm]
Bullen Cave	SEMP	063/68	Strike slip sinistral	150
Emmerberg Cave	SEMP	162/77	Strike slip sinistral	39
Zederhaus Cave	MM	324/86	Strike slip sinistral	10
Eisenstein Cave	VBT	090/70	Normal	~750
Geierkogel Cave	LA	031/81	Strike slip dextral	40
Obir Cave	PAL	162/68	Strike slip sinistral, normal	130

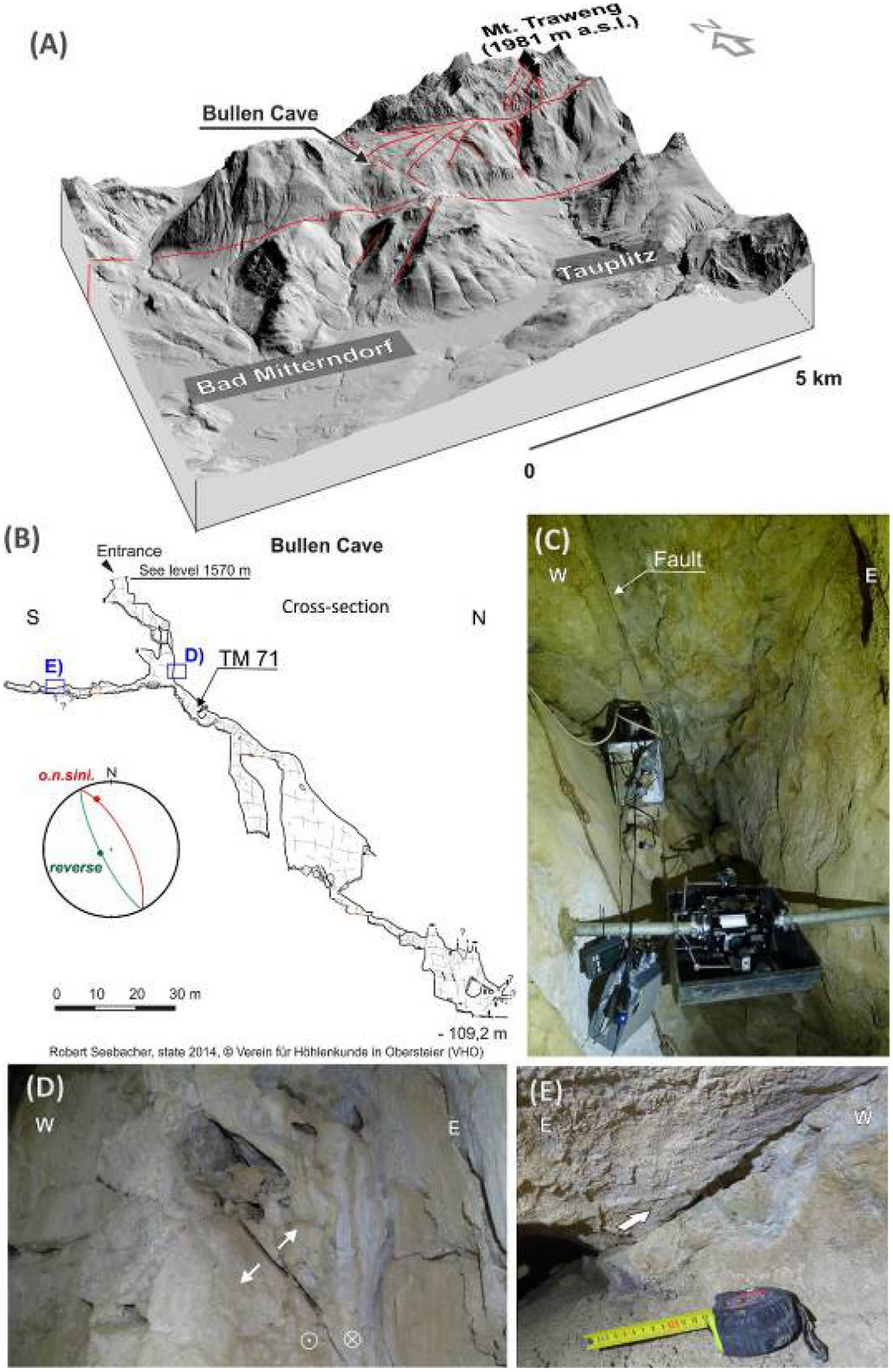

Fig. 2. Local settings of the Bullen Cave site: (A) oblique 3D view of hillshaded digital terrain model with illumination from SE with depicted brittle faults; (B) Map of Bullen Cave (after Seebacher, 2014) with position of TM71 device, monitored strike slip fault (red) and another active reverse fault projected on the lower hemisphere; (C) photo of the monitored active strike-slip fault with the recent offset of 5 cm and with the TMT1 station; (D) opening of the monitored fault due to its curvature indicating hanging-wall upward component; (E) active reverse fault 243/77° with an active offset of 1.3 cm along a vector 250/76. (For interpretation of the references to colour in this figure legend, the reader is referred to the web version of this article.)

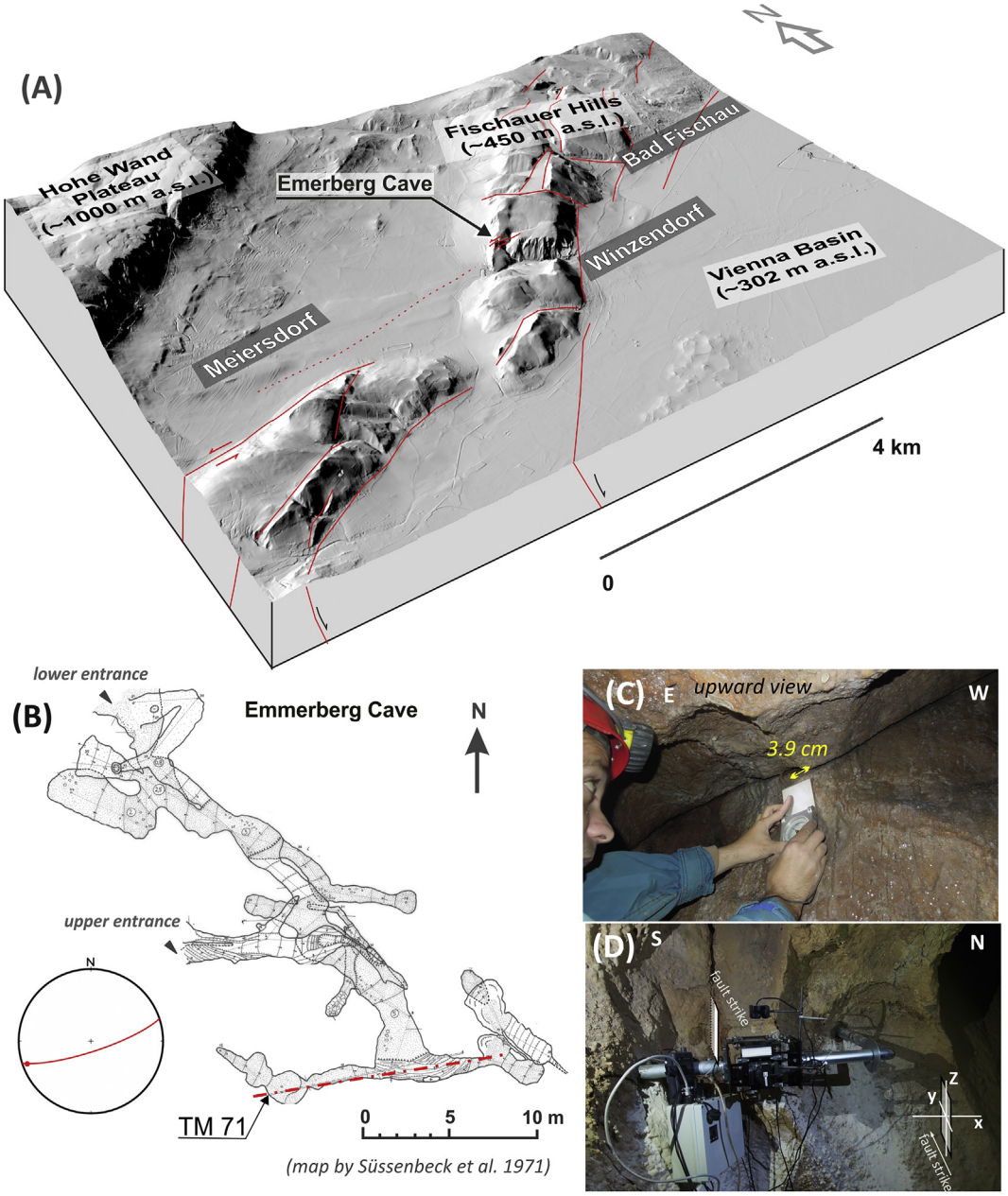

Fig. 3. Local settings of the Emmerberg Cave site: (A) oblique 3D view of hillshaded digital terrain model with illumination from NW with distinct brittle faults; (B) Map of Emmerberg Cave (after Süssenbeck et al., 1971) with depicted position of TM71 device and stereographic projection of the monitored active sinistral strike slip fault (red); (C) photo of the monitored active strike-slip fault with the recent offset of 1 cm; (D) detail of TM71 device. (For interpretation of the references to colour in this figure legend, the reader is referred to the web version of this article.)

East (Fig. 1). The first is situated in Bullen Cave in the southern part of the Totes Gebirge Mts., about 10 km North of SEMP fault near Tauplitz (Fig. 2A). The cave consists of a series of vadose pits and inclined passages with a length of 591 m and a depth of 182 m (Fig. 2B). The vertical entrance opens at 1570 m asl. and the monitored site is placed at −35 m below the ground surface. The room with the device is climatically stable with temperature variations of only 1.3 °C between the measurements. Two distinct faults in the cave reveal signs of recent activity (Fig. 2B). The monitored fault (Fig. 2C) is oriented 063/68° (dip direction/dip angle) with a total macroscopic 4 cm active sinistral strike-slip offset of the cave morphology (deeper in the cave it is up to 15 cm). The recent faulting consisted of two distinct phases; the sinistral one had a normal component and the second younger one comprised an upward component of the north-eastern block indicated by a 1 cm wide void between the fault planes (Fig. 2D). Another macroscopically active fault is a reverse fault 243/77° with striations 250/76° and a cave-wall offset of 1.3 cm (Fig. 2E).

The easternmost termination of SEMP close to the Vienna Basin is monitored in Emmerberg Cave (Figs. 1, 3A). The cave is 150 m long and 23 m deep and it opens at 430 m asl. on the edge of the Fischauer Hills separating the Neue Welt Basin and the Vienna Basin (Fig. 3B). The genesis of the cave is a matter of discussions as it reveals some morphologic hints for hydrothermal control, and clastic sediments composed of Cretaceous rock fragments indicate an epigean influence of allochthonous inflow. The most remote passage of the cave is dissected by a sinistral strike-slip fault 162/77° (Fig. 3B) with an active offset younger than the dissolutional cave wall by 3.9 cm along the vector 252/05° (Table 1, Fig. 3C, D). The fault is straight, open by few mm, partly filled with reddish clay. It has no distinct *syn*-tectonic mineralization and is parallel to the master SEMP fault (Baroň et al., 2016).

The monitored site is climatically stable with variations of less than 0.8 °C between individual measurements.

3.2. Mur-Mürz (MM) fault system

The Mur-Mürz fault system stretches from the Fohnsdorf Basin in the SW for about 130 km to the southern margin of the Vienna Basin in the NE (Fig. 1; Frisch et al., 2000). Generally, it forms a wide valley along the Mur and the Mürz Rivers. The sinistral system formed several small pull-apart basins where sedimentation dates back to Lower Miocene (Carpathian, ca. 17 Ma) giving the onset of the fault movement. A total displacement of 40 km is estimated by Linzer et al. (2002). Basili et al. (2013) estimated a 1.0 to 2.0 mm/yr displacement rate for the eastern part of the MM fault system, while the GNSS based model by Umnig and Weber (2017) estimates the rate by 0.4 mm/yr. The area near the Semmering Pass belongs to the zones with high seismic hazard in the Eastern Alps (Lenhardt, 1995). Our analysis of the digital terrain model reveals that the generally transtensional strike-slip MM fault system suddenly shows hints of transpression or compression at the Semmering Pass, while further to the NNE it immediately transfers into the pull-apart Vienna Basin.

The TM71 device was installed in Zederhaus Cave located within a broad fault zone about 7 km WSW from the Semmering Pass (Figs. 1, 4A). This 57 m long and 19 m deep cave is developed in Upper Triassic marble of the Upper Austroalpine Unit. The main entrance opens at 915 m asl. in a steep slope about 120 m above the valley floor at MM fault. Two distinct active brittle faults were documented in the cave (Fig. 4B). We have monitored the 324/86° sinistral strike-slip fault with a macroscopic offset of 1 cm that strikes subparallel to the master MM fault (Table 1, Fig. 4C, D). Another distinct active fault of dip direction and dip angle of 105/81° revealed a dextral oblique normal offset by 48 cm along the vector 195/14° (Fig. 4E), which is atypical in this area and difficult to interpret within the recent stress field. As the small cave has four entrances, the thermal differences reach up to 4 °C having a direct effect on the monitoring results.

3.3. Vienna Basin Transfer (VBT) fault

The NNE-SSW striking and 200 km long VBT fault system is a northeastern continuation of the MM fault system. It comprises several strike-slip and normal faults associated to the rhomboidal pull-apart Vienna Basin. The sinistral strike-slip faults are striking NE-SW and the normal faults at the outline of the basin associated with the subsidence of the basin are striking NNE-SSW (Decker, 1996). The trace of VBT stretches from the MM fault across the Danube River up to NW Slovakia. The fault originated during the Middle Miocene (Badenian, ca. 16 Ma) until the Upper Miocene (8 Ma) (Decker, 1996; Peresson and Decker, 1997; Hölzel et al., 2010). The ongoing Quaternary tectonic activity is evidenced by the Pleistocene terraces and Quaternary basin sediments (Decker et al., 2005; Beidinger and Decker, 2011).

Eisenstein Cave is situated at Emmerberg Cave's opposite slope of the Fischauer Hills at an altitude of 380 m asl. The slope is facing the Vienna Basin near its suspected western marginal faults (Fig. 5A). The 2.3 km-long cave developed in limestone breccia and sandstone of Middle Miocene age; it has a crevice character along a N-S-oriented fracture parallel to the fault scarp of the Vienna Basin (Fig. 5B and C). The cave is partly filled by numerous blocks and boulders that result in a complex maze. The northern part of the cave collapsed, most probably because of a deep-seated rockslide to the North of the cave. The deepest parts of the cave reach a hydrothermal water level 73 m below the entrance. The 15.5 °C hydrothermal spring, high CO_2 content in the air (up to 2%), characteristic morphologic features, and speleothems indicate phases of a hypogene speleogenesis or at least overprint (Plan et al., 2009; Baroň et al., 2016). The water level and temperature of the lake variate probably also in response to regional tectonic processes (Hardege, 2018). The TM71 extensometer is located in the approximate centre of the cave, where the original fracture was best preserved (Table 1, Fig. 5D).

3.4. (Pöls-)Lavanttal (LA) fault system

The NNW-SSE oriented fault system is about 150 km long and strikes NNW-SSE from Pöls Valley, through the Lavant Valley to Slovenia. The northern part of the system is composed of the Pöls Fault. At the transition of the Pöls fault to the LA fault, the dextral strike-slip system strikes NW-SE and locally forms an uplifting transpressional zone near Judenburg. Here it forms a hilly range of a positive flower structure including the inversion of the SW part of the Miocene Fohnsdorf Basin (Sachsenhofer et al., 2000). This transpressional zone is also seismically active with relatively high seismic hazard (Lenhardt, 1995). To the SE the fault system continues into the Lavant Valley and further to Slovenia, where it is cut by the Periadriatic and Sava-Šoštanj-Donat Fault Systems (Decker et al., 1994; Linzer et al., 2002; Kurz et al., 2011; Fodor et al., 1998). The main activity with dextral strike-slip kinematics dates back to Miocene and Pliocene times. The horizontal offset is estimated to be 10–18 km (Fodor et al., 1998; Linzer et al., 2002) and the vertical offset to 2–5 km (Kurz et al., 2011). The GNSS based model by Serpelloni et al. (2016) provides a right-lateral, transpressive motion with a strike-slip rate of 0.5 ± 0.1 mm/yr, while Vrabec et al. (2006) estimated a displacement rate of 1.0 to 2.0 mm/yr.

The monitored fault 031/81° is located in Geierkogel Cave south of Judenburg within the above mentioned transpressional zone (Table 1, Fig. 6A). This fossil relict phreatic karst cave is developed in Paleo- and Mesozoic marbles at a small plateau bordered by steep scarps probably associated to faults. The cave is 150 m long, 22 m deep and its 5 m-deep entrance pit is situated at 910 m asl. A dextral strike-slip fault of 218/74° (dip angle and dip direction) is exposed at the entrance chamber and reveals oblique dextral normal and reverse dextral activity phases (Fig. 6B). The major active fault 031/81° dissects and offsets this passage dextrally for about 4 cm. The TM71 device could be only situated at a place, where also a huge 15–20 m-long block is detached from the cave wall (Fig. 6C), that according to the kinematic markers on the cave surface rotates within the fault zone counterclockwise, but the field inspection proves that it is not a simple gravitational topple. Observed temperature variations are less than 0.2 °C.

3.5. Periadriatic Line (PAL) fault system

The fault system of the ESE-WNW trending PAL forms the border between the Eastern and the Southern Alps (Schönlaub and Schuster, 2015). In the eastern part, the fault system strikes in the E-W direction and the dextral fault forms a large transpressional duplex of the Karawank Mts. (Poltnig and Herlec, 2012). The recent dextral movement started ca. 17 Ma ago, as the fault system was reactivated by the N-S shortening of the Eastern Alps compensated by the lateral extrusion (Ratschbacher et al., 1991). The dextral offset of PAL is estimated to be several tens of km (Schönlaub and Schuster, 2015). The Karawank Mts. have been uplifted recently and thrusted over the Neogene and even Quaternary sediments of the Klagenfurt basin to the North. About 12 Ma ago (Middle Miocene, Sarmatian), the Karawank Mts. did not exist as mountains (Poltnig and Herlec, 2012). Vrabec et al. (2006) estimated a 1.2 mm/yr present-day displacement rate of the PAL fault system.

East of Mt. Obir within this transpressional zone, a conjugate left-lateral fault system strikes ENE-WSW north of the PAL fault core. This conspicuous fault is well visible on the high resolution ALS digital terrain models (Fig. 7A); here we call it the Obir Fault. Unfortunately, only later in course of the project we identified that the SE slopes of the mountain ridge dissected by the Obir fault are also occupied by very deep-seated gravitational slope deformation (DSGSD) with rugged topography, bulging and pressure ridges along the toe, and sagging in the upper portion.

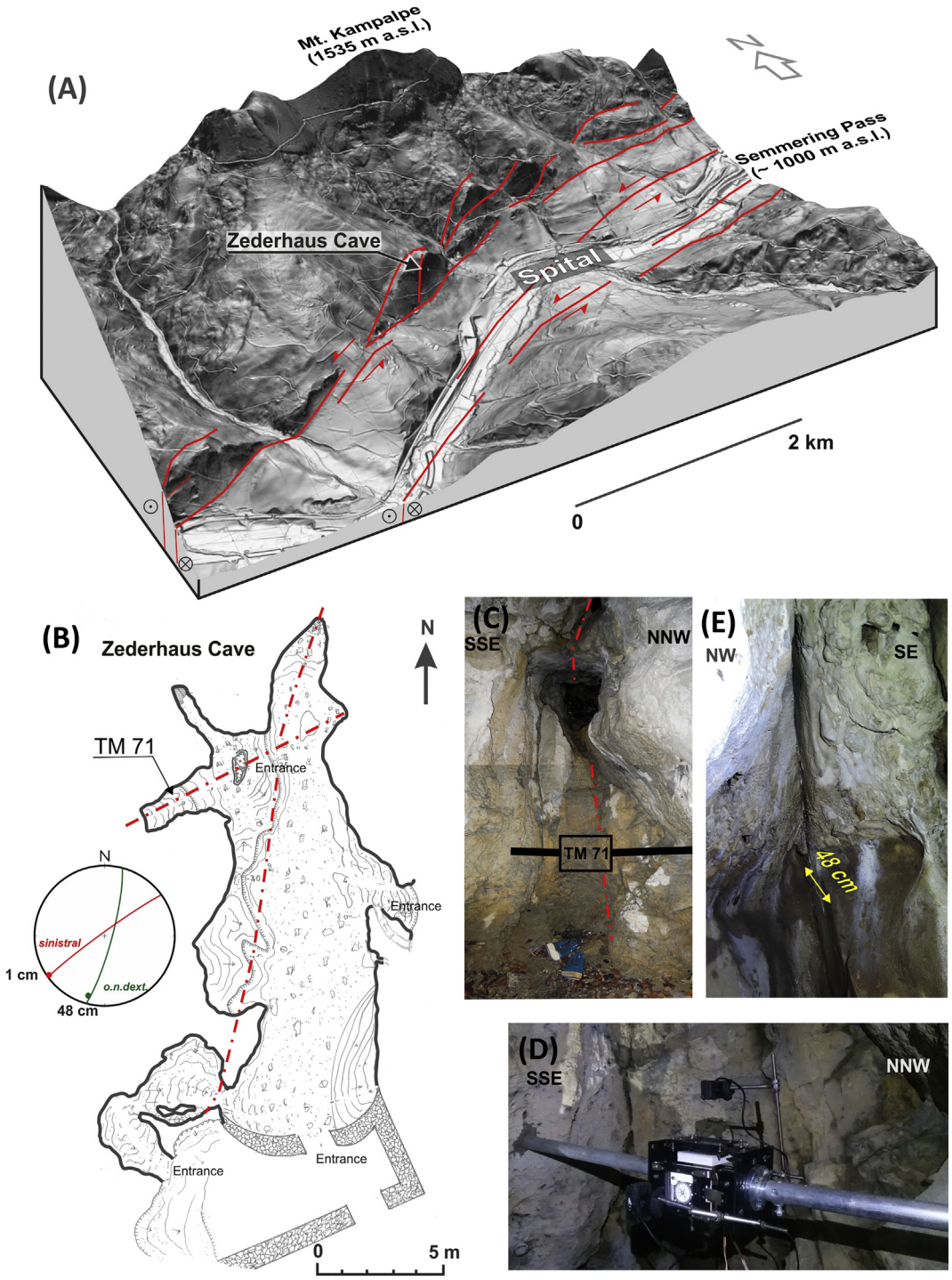

Fig. 4. Local settings of the Zederhaus Cave site: (A) oblique 3D view of the slope map from digital terrain model with depicted major brittle faults; (B) Map of Zederhaus Cave (after Schmied and Schmied, 1975) with depicted position of TM71 device and stereographic projection of the monitored sinistral strike slip fault (red) and another active oblique normal dextral fault; (C) photo of the monitored strike-slip fault with the recent offset of 1 cm; (D) detail of TM71 device; (E) photo of the oblique normal dextral active fault. (For interpretation of the references to colour in this figure legend, the reader is referred to the web version of this article.)

The monitored site, attributed to the Obir fault, lies in the Wartburg chamber in Obir Caves NW of Bad Eisenkappel and SW of Zauchen village (Fig. 7B). The caves were discovered by lead-zinc mining (Spötl et al., 2005) and were established as a show cave in 1991. Most probably the caves are of a hypogean and phreatic origin with a minor vadose overprint. They have developed within a tectonic fragment of Middle Triassic Wetterstein limestone (Poltnig and Herlec, 2012). The active faults in Wartburg chamber consist of several dislocations with a distinct offset of the cave solutional surfaces. We have been monitoring two of them with TM71 devices at OBI1 and OBI2 faults, respectively. The OBI1 fault is exposed for approximately fifty meters with the fault surface orientation 150°/72° and approximately 38 cm of total active sinistral offset and an aperture between the fault blocks generally around 4 mm. During a minor younger reactivation, the fault moved as an oblique reverse dextral one for few cm. On the other hand, the OBI2 station was placed at a 1.5 m wide cataclastic intersection of a strike-slip (162/68°) and oblique reverse (162/87°) faults with striations and tectonic mirrors, and with about 13 cm post-speleogenetic offset

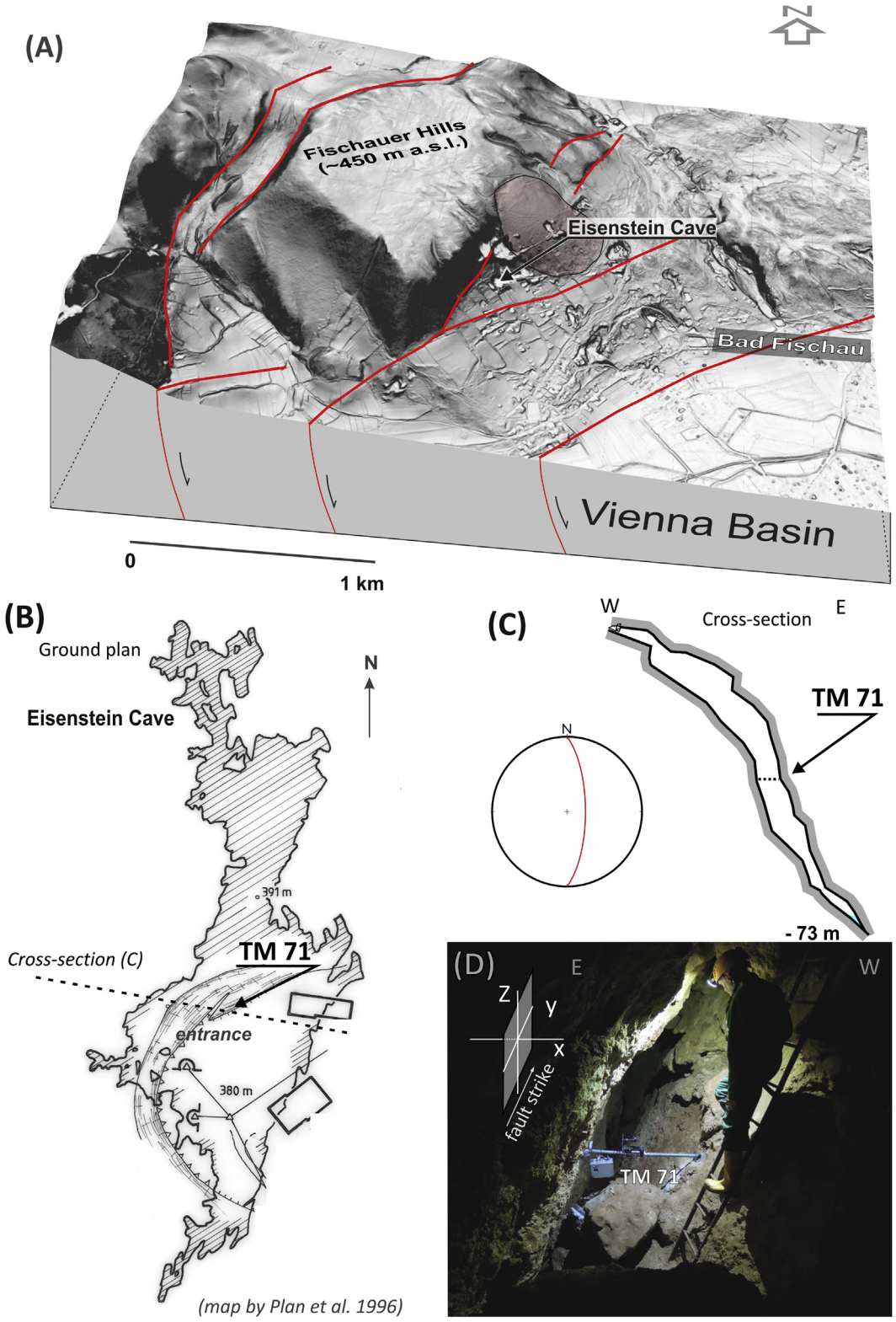

Fig. 5. Local settings of the Eisenstein Cave site: (A) oblique 3D view of the slope map from digital terrain model with depicted location of the cave, distinct brittle faults and deep-seated rockslide (red area); (B) Map and (C) cross-section of Eisenstein Cave (after Plan et al., 1996) with depicted position of TM71 device and stereographic projection of the fault, (D) photo of the monitored active tectonic crevice and TM71 extensometer. (For interpretation of the references to colour in this figure legend, the reader is referred to the web version of this article.)

(Table 1, Fig. 7C); common features are crack openings, fresh rock crushing, rock falls, and speleothem damage. Other irregular rough and open fractures are probably attributed to the gravitational slope failure. The OBI1 station had been affected by several technical failures due to high cave-air moisture causing damage of electronic elements. Therefore, it had registered only sporadic displacement events in course of observation and we do not present the incomplete longer time series here.

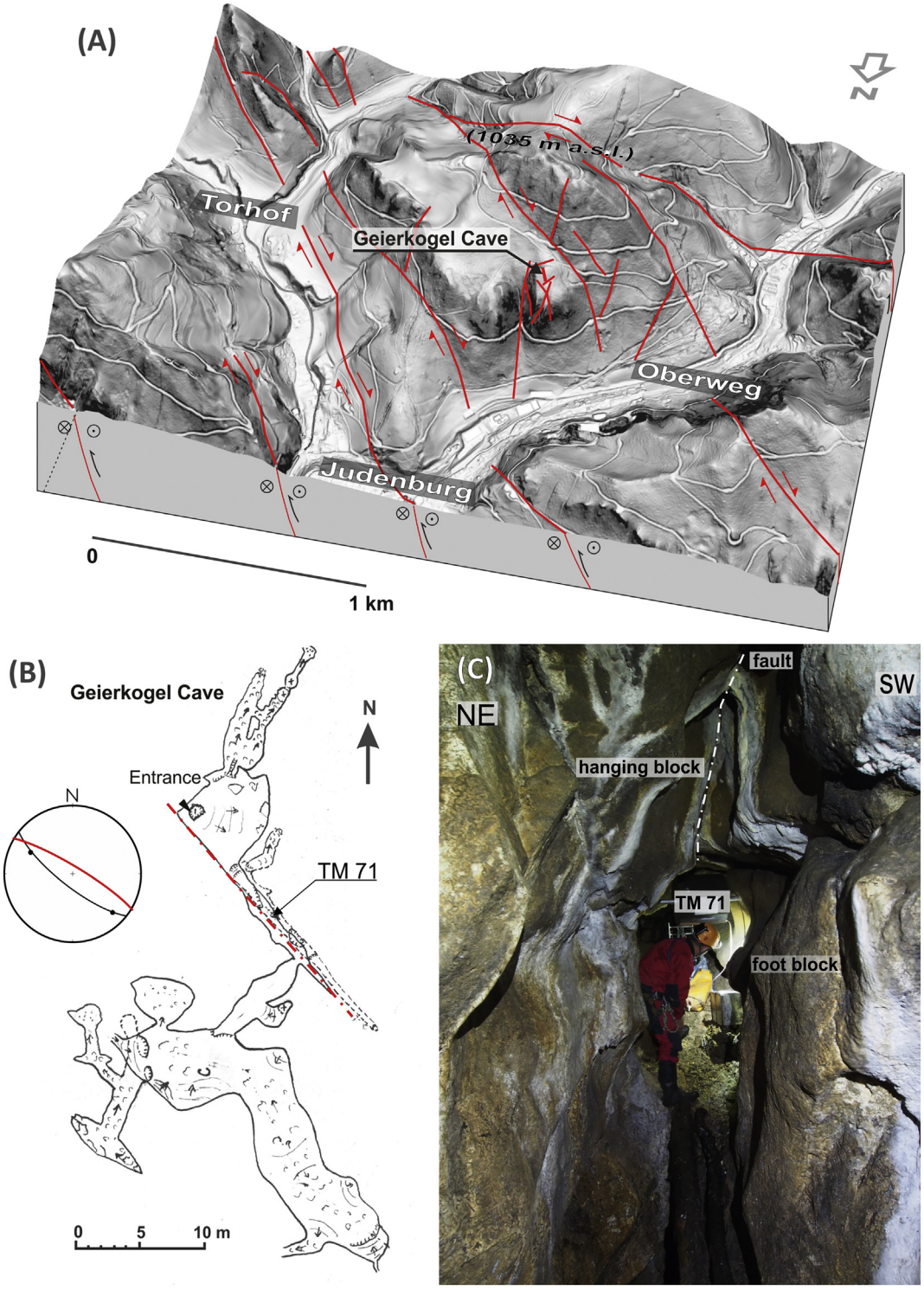

Fig. 6. Local settings of the Geierkogel Cave site: (A) oblique 3D view of the slope map from digital terrain model with depicted location of the cave and brittle faults; (B) Map of Geierkogel Cave (after von Czoernig-Czernhausen, 1924) with depicted position of TM71, monitored active dextral strike slip fault (red) and another polyphaser dextral oblique reverse and normal fault (black) projected on the lower hemisphere; (C) photo of a cave passage with the monitored active strike-slip fault. (For interpretation of the references to colour in this figure legend, the reader is referred to the web version of this article.)

3.6. Seismicity in course of the project

Although the Eastern Alps and Eastern Austria show low to moderate seismicity (Apoloner et al., 2014), several very weak to moderate earthquakes with magnitudes ranging from 0.01 to 4.1 were registered in close vicinity of the study sites in the course of the project (earthquake catalogue by ZAMG). Particularly distinct earthquakes are presented in Fig. 8 and commented alongside the results in the text below.

4. Results

All the monitored faults revealed evidences of ongoing active movements. In the following we describe the events and general

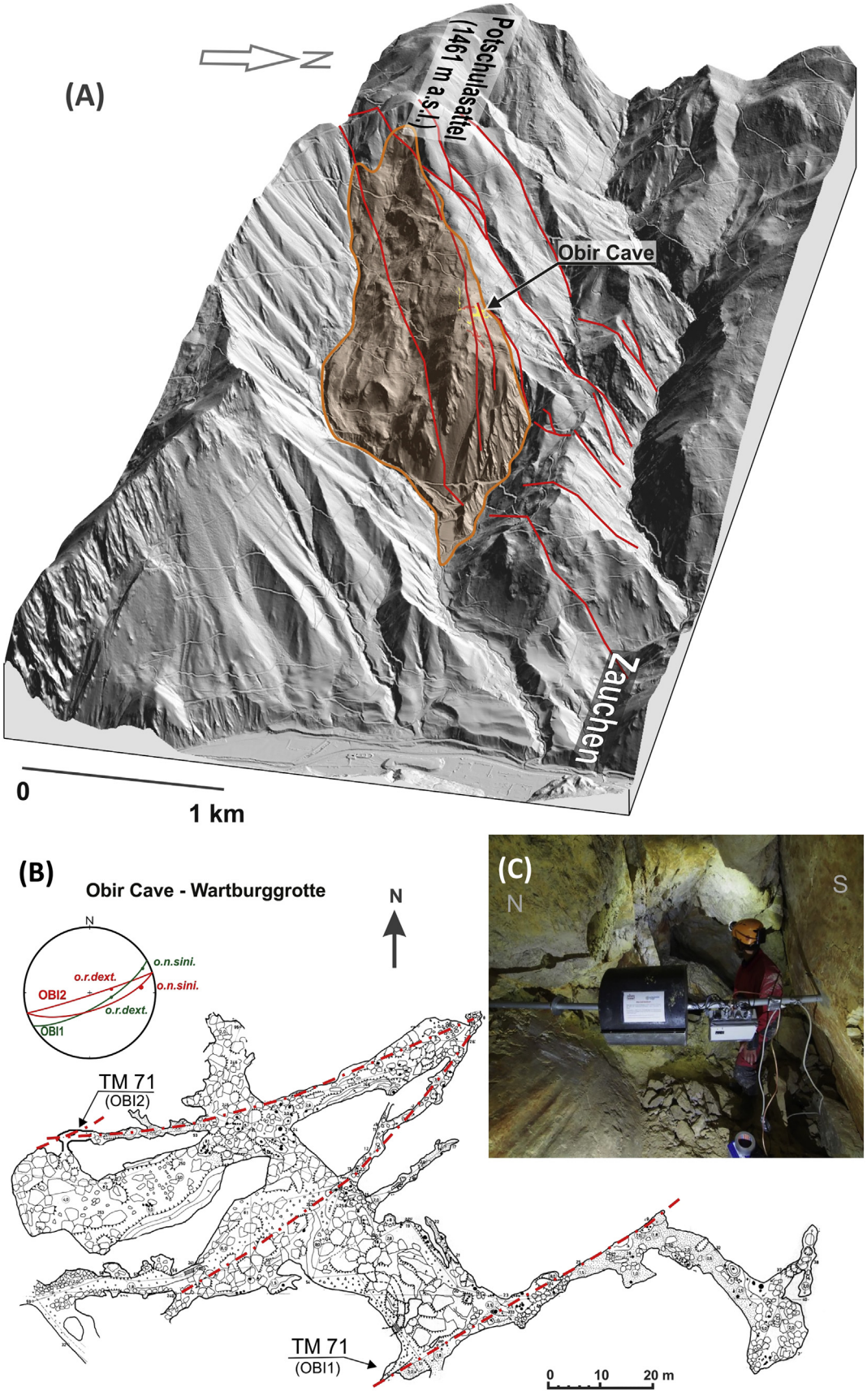

Fig. 7. Local settings of the Obir Cave site: (A) oblique 3D view of the hillshaded digital terrain model illuminated from NW with depicted Obir fault system conjugated to PAL fault and deep-seated gravitational slope deformation (orange area); (B) Map of the Wartburggrotte part of Obir Cave (after Solar et al., 1970) with depicted position of TM71 devices, monitored active oblique normal sinistral and oblique reverse dextral faults at OBI2 (red) and polyphase active oblique normal sinistral and oblique reverse dextral fault at OBI1 (green) projected on the lower hemisphere; (C) photo of the monitored active cataclastic zone of strike-slip faults at OBI2 with the recent offset of up to 13 cm. (For interpretation of the references to colour in this figure legend, the reader is referred to the web version of this article.)

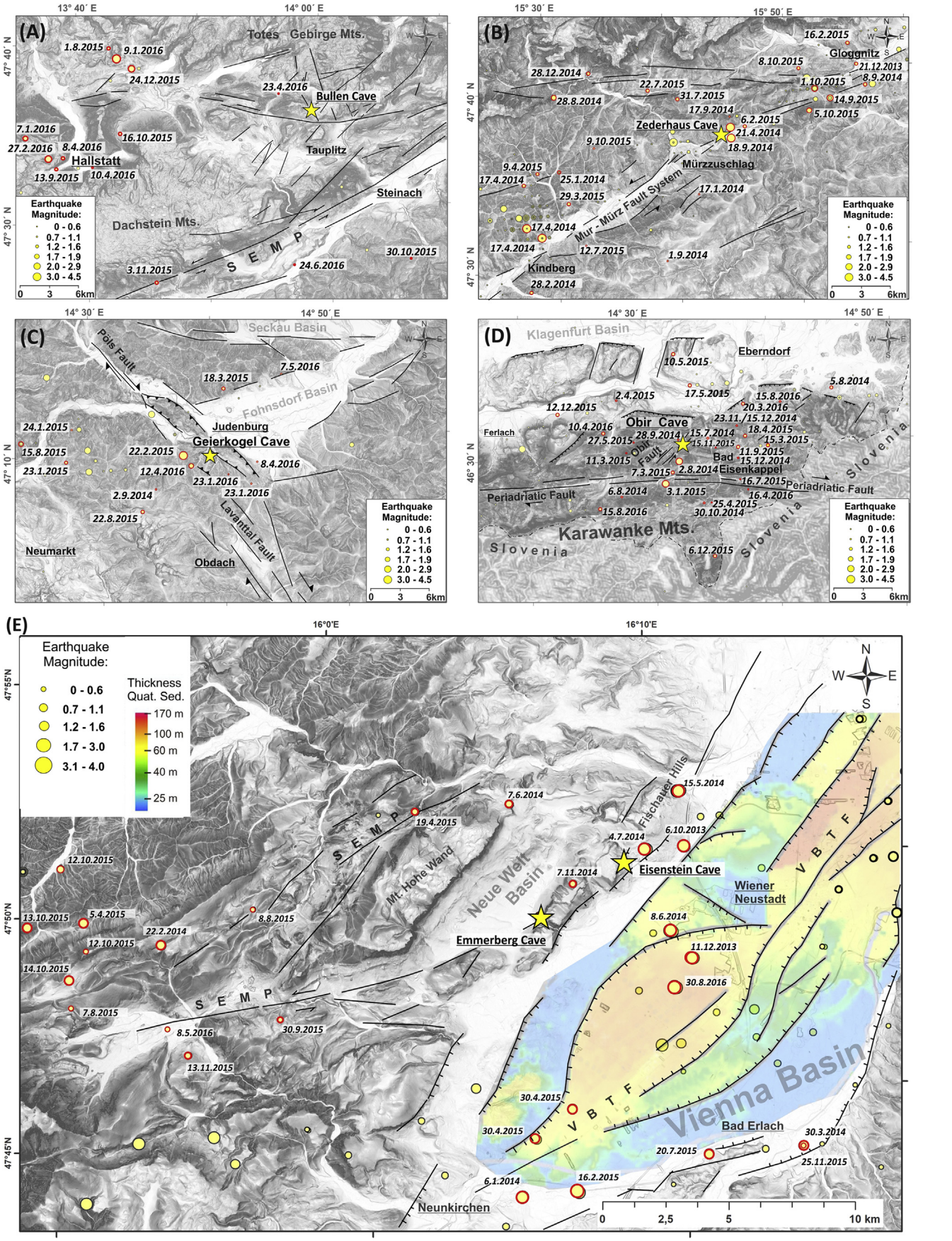

(caption on next page)

Fig. 8. Map of local earthquakes adjacent to monitored faults in course of observation: (A) Bullen Cave adjacent to SEMP fault system central part, (B) Zederhaus Cave at the Mur-Mürz fault system, (C) Geierkogel Cave within the zone of transpression of the Pöls-Lavanttal fault system, (D) Obir Cave within the zone of transpression of the Periadriatic fault system, and (E) Emmerberg and Eisenstein Caves at SEMP and Vienna Basin Transfer faults. Topography: slope map from digital terrain models from 10 m resolution airborne laserscan data (courtesy of government of Austria), Seismicity: Austrian earthquake catalogue (Courtesy: ZAMG Vienna), Thickness of Quaternary sediments in Vienna Basin after Salcher et al. (2012).

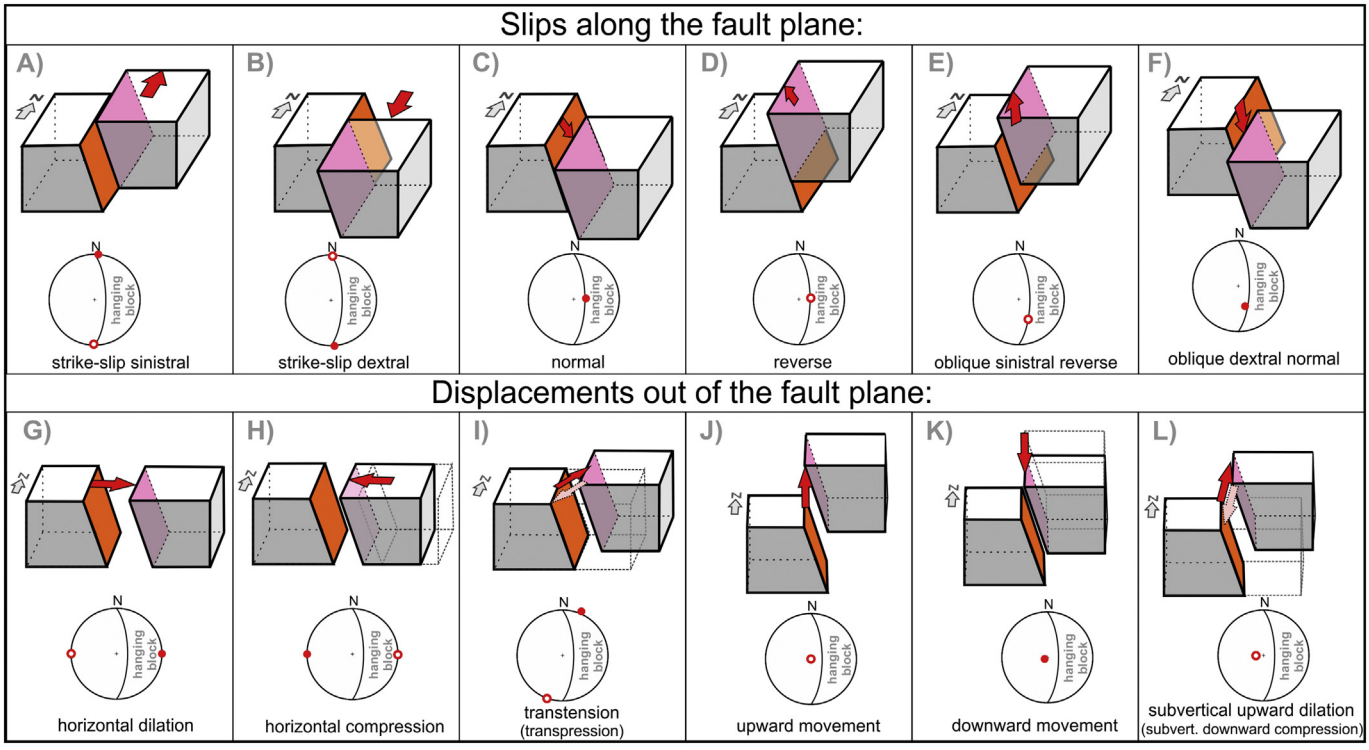

Fig. 9. Review of fault displacement patterns and their stereographic projection on lower hemisphere.

Table 2
Review of fault activity parameters.

Location	Fault	Duration of observation [months]	Nr. of events	Dc vector trend/plunge [°]	Dc [mm]	Ds [mm]	Ip [Dc/Ds]	Dc rate/year [mm]
Bullen Cave	SEMP	13	10	097/−45	0.062	0.091	0.68	0.057
Emmerberg Cave	SEMP	29	19	209/31	0.040	0.105	0.38	0.017
Zederhaus Cave	MM	22	513	288/29	0.351	5.429	0.09	0.191
Eisenstein Cave	VBT	24	5	106/61	0.052	0.063	0.81	0.026
Geierkogel Cave	LA	24	28	005/−06	0.009	0.165	0.05	0.005
Obir Cave	PAL	22	55	159/22	0.095	0.295	0.32	0.052

Explanations: Dc – cumulative displacement, Ds – sum of all displacements' absolute values, Ip – index of periodicity.

displacement pattern (Fig. 9) and trends (see Table 2). We registered fault slips along the particular fault plane, i.e.: strike slips, normal and reverse slips, and oblique ones (Fig. 9A–F) and the displacements of the hanging block out of the fault plane, i.e.: horizontal dilation and compression, horizontal (and oblique) transtension and transpression, hanging block upward and downward movement and subvertical upward dilation or subvertical downward compression (Fig. 9G–L).

4.1. Bullen Cave (SEMP fault system)

In course of the observation period from 1 June 2015 to 31 August 2016, ten fault displacement events were registered on the monitored fault in the Bullen Cave. The total cumulative displacement (*Dc*) within this period was 0.062 mm, while the total sum of all individual displacement events (*Ds*) was 0.091 mm. The thermal effect was almost negligible as the temperature variations (ΔT) were less than 1 °C between single measurements (Fig. 10). It was confirmed also by the index of periodicity (*Ip* = 0.68) (Table 2). The average annual rate of the cumulative displacement was 0.057 mm/year.

Four remarkable activity phases were observed and the fault revealed a variety of displacements (Fig. 10). None of these displacements coincided with any seismicity registered by ZAMG (Fig. 10).

The first phase lasted from June to July 2015 and was manifested by continuous counter clockwise vertical rotation along Y axis culminating in a sudden distinct subvertical upward movement by 0.024 mm on 21 July 2015 (Fig. 10). A couple of days later, very shallow earthquakes occurred in 22–26 km hypocentral distance at the end of this fault activity phase, i.e.: M = 1.6 EQ on 1st August 2015 north-east of Hallstatt (Fig. 8A) and a M = 1.7 EQ near Sankt Pankraz with hypocentral depths of 3 and 2 km, respectively.

The second phase lasted about seven days and was manifested by distinct upward movement by 0.024 mm on 23 November 2015, similar to the previous phase. The fault activity continued then as tiny dilational, dilational normal and dextral movements with counter clockwise rotations until 30 November 2015. A shallow M = 2 earthquake occurred on 2 December after these displacements about 40 km away

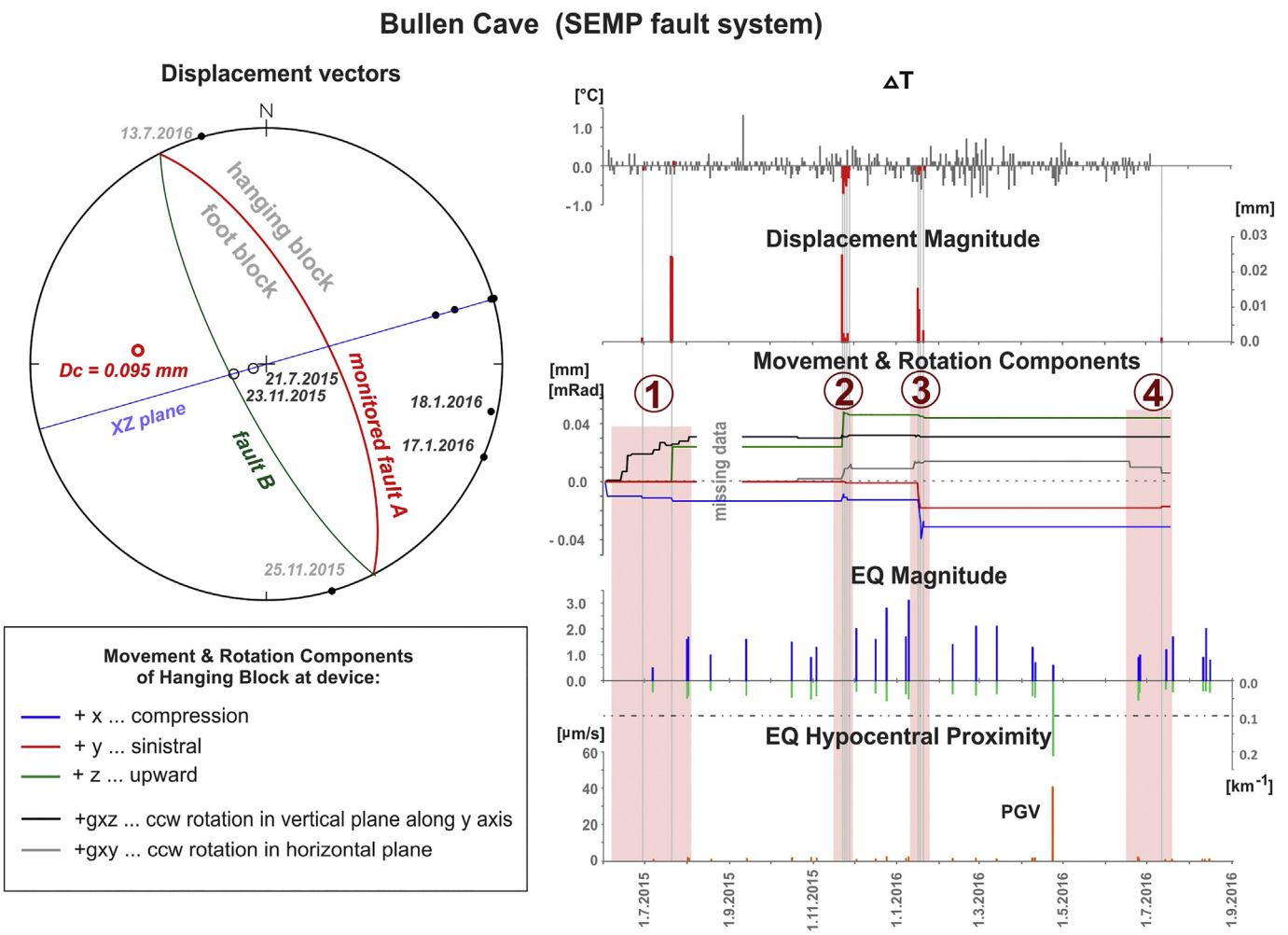

Fig. 10. Review of the fault activity in Bullen Cave (adjacent to SEMP Fault central part) within the period from 1 June 2015 to 31 August 2016: the displacement vectors' orientation, the fault plane and the TM71 device orientation are projected on the stereoplot lower hemisphere (left part of the figure), variation of cave air temperature (ΔT), displacement magnitudes, cumulative values of particular displacement components (x, y, z), block rotations (gxz and gxy) of device and numbered fault-activity phases are to the right. The full circles on the stereoplot represent down-directed movement vectors of the hanging block, the hollow circles are the upward movements of the hanging block projected on the lower hemisphere. Local seismicity (Courtesy: ZAMG Vienna) in course of observation is expressed by earthquake magnitudes (blue graph), hypocentral proximity (green graph) and peak-ground velocities at the fault calculated for each particular earthquake; horizontal double-dot and dashed line indicates hypocentral radius of 10 km. Only remarkable displacements over 0.01 mm are labelled in black in the stereoplot, tiny displacements, surely not caused by thermal variations, are labelled in grey. (For interpretation of the references to colour in this figure legend, the reader is referred to the web version of this article.)

near Aigen-Voglhub.

The third phase was recorded on 14–22 January 2016 after a M = 3 earthquake on 9 January near Altaussee (NE of Hallstatt) about 20 km away (Figs. 8 and 10). The activity phase was represented by tiny hanging-block counter clockwise horizontal rotations and distinct dilational oblique dextral displacements on 17 and 1 January by 0.014 and 0.017 mm, respectively (Fig. 10).

The undistinguished fourth activity period in summer 2016 was manifested only by very tiny clockwise horizontal rotations and a minor sinistral fault movement on 13 July 2016. Only some very weak earthquakes occurred during this phase in hypocentral distances of 35–50 km (Fig. 10).

Surprisingly, a very local earthquake on 23 April 2016 with relatively distinct peak-ground velocity (PGV) had no manifestation in fault activity (Fig. 10).

Tiny horizontal dilations were probably caused by thermal variations. The final vector of the cumulative displacement (Dc) had a component of an oblique extensional upward movement of the hanging block with the orientation of 097/−45, i.e. 277/45 when projected on the lower hemisphere (Table 2, Fig. 10).

4.2. Emmerberg Cave (SEMP fault system)

The observation period in the Emmerberg Cave was the longest and most continuous one and lasted from 15 November 2013 to 31 August 2016 with only some technical failures. Totally 19 displacements were registered on the monitored fault in this period; the total cumulative displacement was relatively low when compared to the other sites (Table 2, Dc = 0.040 mm), while the total sum of all particular displacement events (Ds) was 0.105 mm. The Dc vector was 209/31° oriented with an oblique transtensional dextral component (Fig. 9). The effect of the temperature variations (ΔT) was again almost negligible as they did not exceed 1 °C between single measurements (Fig. 9). The index of periodicity (Ip = 0.38) was the third highest from the monitored sites and the average annual rate of the cumulative displacement was 0.017 mm/year (Table 2).

A variety of displacement modes was characteristic also for this fault. Two distinct and five other less evident activity phases were observed in course of the observation (Fig. 11). The phases were mostly manifested by the fault-block's clockwise and counter clockwise horizontal rotations and tiny displacements near the resolution limit, such

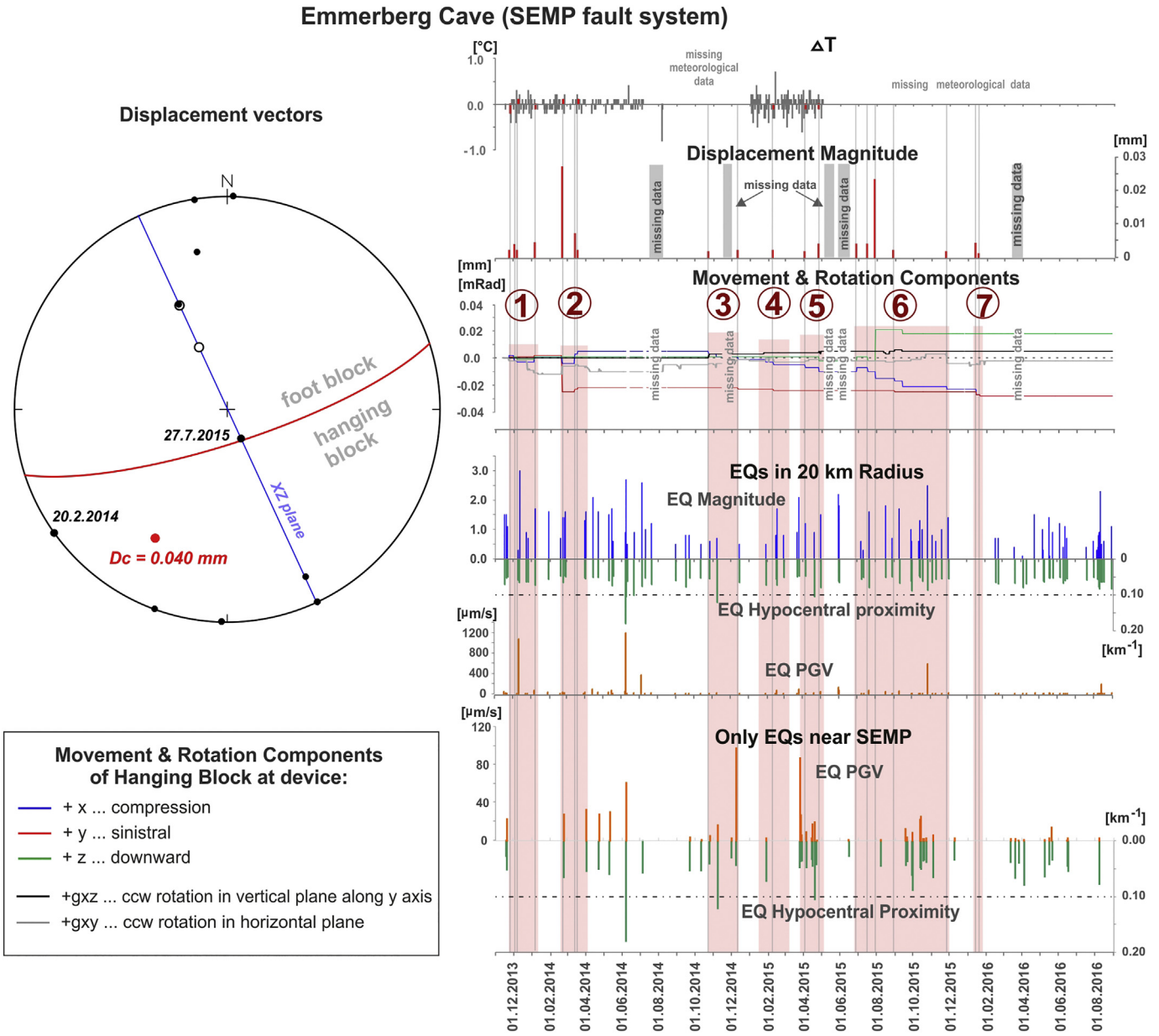

Fig. 11. Review of the fault activity in Emmerberg Cave (SEMP Fault termination part) within the period from 1 November 2013 to 31 August 2016. For details see captions of Fig. 10. Remarkable displacements over 0.01 mm are labelled.

as extension with a normal component, compression, upward compression, dextral transtension, and sinistral transpression (Figs. 8 and 11).

The distinct second phase in February and March 2014 was characterized by a remarkable oblique dextral strike slip with a dilational component by 0.028 mm on 20 February, followed by tiny oblique compressions with minor sinistral components on 13 and 18 March (Fig. 11). The dextral strike slip preceded by two days a very shallow M = 1.4 earthquake at SEMP fault near Gutenstein on 22 February about 15 km to the W (Fig. 8).

Distinct was also the sixth phase in the second half of 2015 (Fig. 11), represented by tiny alternating compressions and dilations and subvertical movements, and remarkable dip-slip normal displacement on 27 July 2015 by 0.024 mm, and culminating with increasing counter clockwise horizontal rotations and abrupt clockwise rotation back to the original state in late November 2015 (Fig. 11).

Except for the last one, the activity phases interplayed with higher local seismicity associated rather with the SEMP fault system, but not VBT fault. However, some very weak nearby earthquakes even at the SEMP fault system had no manifestation in the fault activity (e.g. spring 2014 or spring-summer 2016); these weak earthquakes had also very undistinguished PGV effect on the site (Fig. 11).

4.3. Zederhaus Cave (MM fault system)

The highest fault activity so far was observed in Zederhaus Cave at the MM fault system. Totally 513 fault displacement events were registered within the period between 1 December 2013 and 15 November 2015. The total sum of all displacement events (*Ds*) was 5.429 mm, whereas the cumulative displacement (*Dc*) was 0.351 mm (Table 2). The orientation of the cumulative displacement was 288/29° (transtensional sinistral strike-slip) and the average annual rate of the cumulative displacement was 0.191 mm/year. Due to dynamic cave climate, the thermal variability between individual measurements was high reaching up to 5 °C; also the index of periodicity was *Ip* = 0.09. The displacement events occurrence was distributed more or less

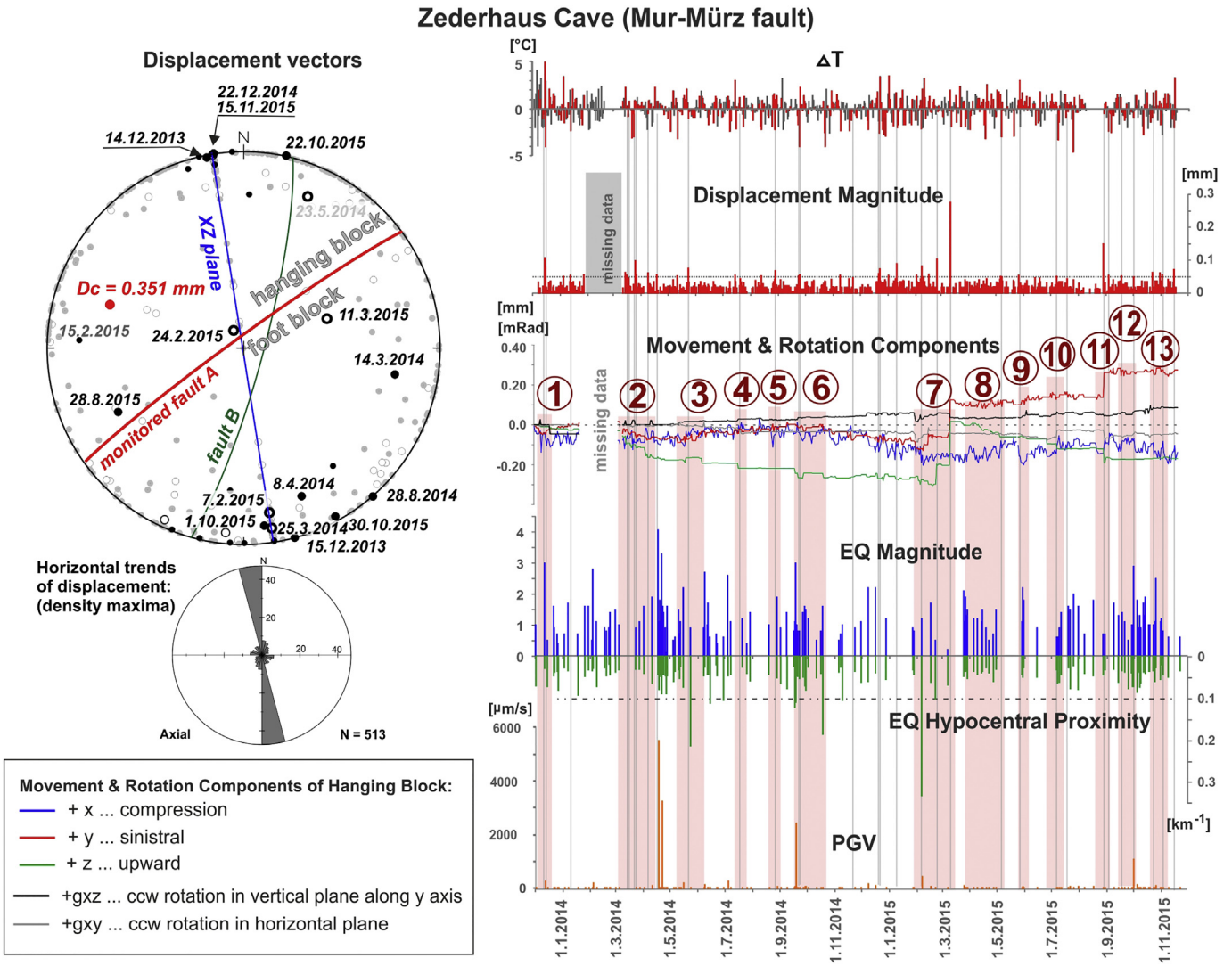

Fig. 12. Review of the fault activity in Zederhaus Cave (Mur-Mürz Fault) within the period from 1 December 2013 to 31 August 2016. For details see captions of Fig. 10. Black dots and circles in the stereoplot – displacements over 0.05 mm, grey ones – displacements below 0.05 mm; only remarkable displacements over 0.06 mm are labelled. The rose diagram presents horizontal trends of all displacements.

continuously over the whole period and clear spatial alignment of the horizontal trends along the X axis indicates a strong effect of thermal variations on the device (Fig. 12).

Despite of that, jumps along the y and z axes (resistant to thermal expansion) and a broad variety of displacement modes revealed several real fault displacement phases (Fig. 12). Some of them were undistinguished, but a few of them manifested distinct changes of the fault behaviour, such as the second, sixth, seventh and eleventh ones in Fig. 12, which we describe in more detail below.

The second phase in March and April 2014 was, in general, manifested by continuous oblique normal dextral trends till mid of April. The period culminated on 17 and 21 April by a series of distinct local earthquakes at MM fault with strong PGV values (Fig. 12). A doublet of relatively strong M = 4.1 and M = 3.5 earthquakes occurred on 17 April near Kindberg, about 24 km SE of the monitored site (Fig. 8); another M = 3.3 earthquake hit on 21 April 2014 in the immediate vicinity with an epicentral distance of roughly 0.8 km from the cave and a focal depth of 11 km. This latter earthquake terminated this fault activity phase.

The sixth phase in September/October 2014 was mostly manifested by dip-slip movements following another distinct local Ml = 1.1 and M = 3.3 earthquakes on 17 and 18 September 2014, with the epicentral distances 1.7 and 1 km and hypocentral distances 8 and 9 km, respectively.

The seventh phase in February/March 2015 started with oblique sinistral normal movements, until a very near M = 1.2 earthquake occurred on 6 February 2015 about 2.2 km to the East of the cave at a depth of 2 km. After this earthquake, the hanging block started to generally move in subhorizontal upward sinistral dilation mode. The maximum displacement was recorded on 11 March, when the hanging block revealed transtensional oblique upward sinistral movement by 0.273 mm (Fig. 12).

And finally, during the eleventh phase at the end of August 2015, the hanging block suddenly moved as an oblique normal sinistral strike-slip (with a minor dilation) by 0.148 mm on 28 August. This phase had no specific seismic manifestation. Another local M = 2.9 earthquake occurred near the Semmering pass on 1 October 2015 in a hypocentral distance of about 13 km with remarkable PGV values (Fig. 12).

4.4. Eisenstein Cave (VBT fault)

Only five fault-displacement events concentrated in three distinct phases were recorded in Eisenstein Cave adjacent to the VBT fault between 1 November 2013 and 31 August 2016 (Fig. 13). About 30% of

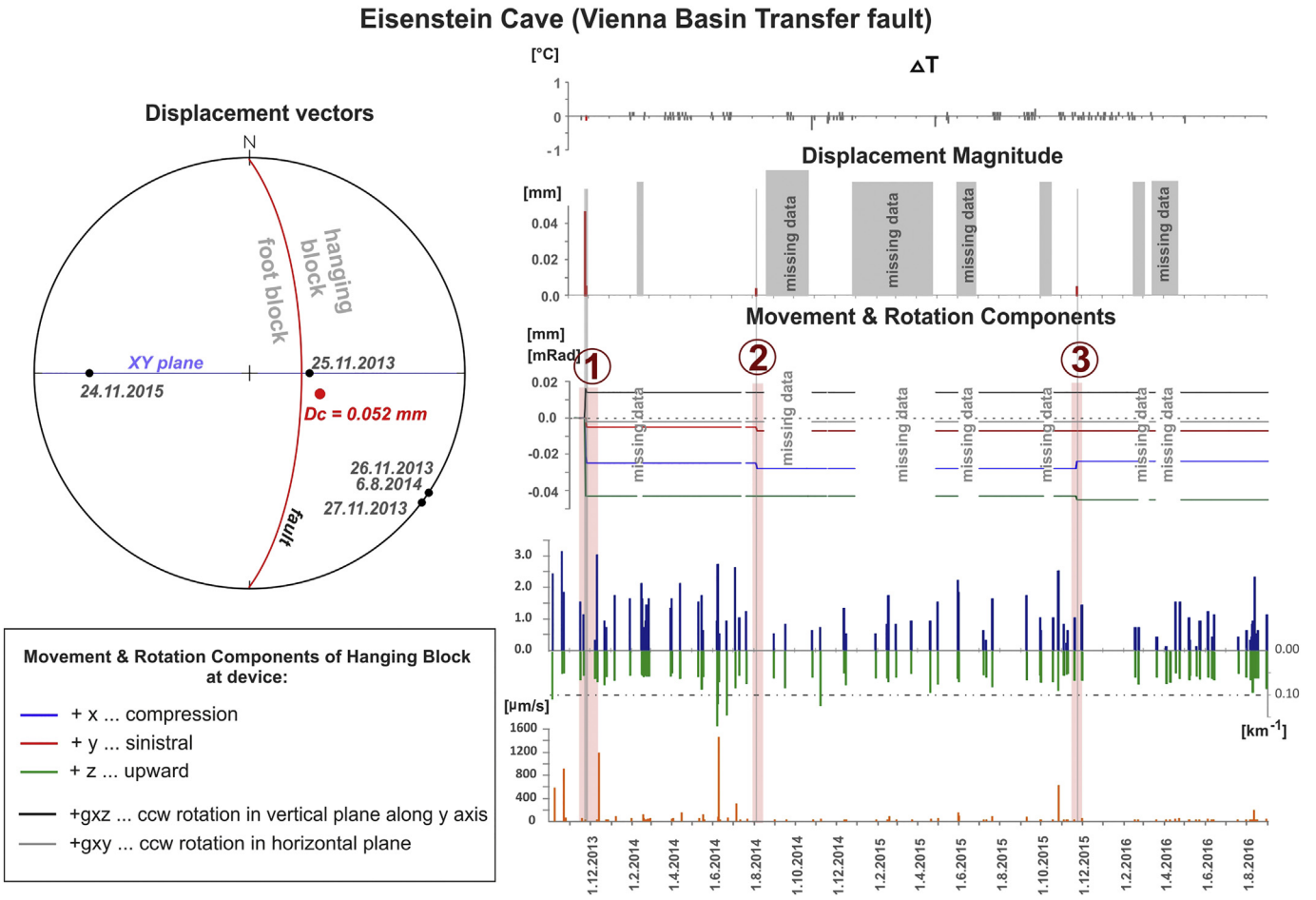

Fig. 13. Review of the fault activity in Eisenstein Cave (Vienna Basin Transform Fault) within the period from 1 November 2013 to 31 August 2016. For details see captions of Fig. 10.

the observation period was affected by technical failures due to high air moisture and CO_2 content in the cave air damaging the electronic parts of TM71 device, but careful image control before/after each device manipulation avoided biasing the results with artificial movements. The total sum of all displacements (*Ds*) was 0.063 mm and the cumulative displacement (Dc) was 0.052 mm with the vector orientation 106/61° (Table 2). The index of periodicity (*Ip* = 0.81) revealed the relatively irreversible nature of the displacement. The annual mean displacement rate revealed a 0.026 mm/year subsidence of the eastern block towards the Vienna Basin.

The first activity phase in November 2013 mostly comprised normal dip-slip displacement by 0.047 mm on 25 November 2013. Other minor following displacements were dextral transtensional dilations on 26 and 27 November 2013. This distinct activity happened at the turn of a seismically relatively high active period in autumn 2013, when two distinct earthquakes occurred in the adjacent Southern Vienna Basin. The strongest one (M = 4.3) occurred near Ebreichsdorf on 20 September 2013 and the other one (M = 4.2) on 2 October 2013, with the hypocentral distances to Eisenstein Cave of 25.8 and 25.1 km, respectively. Another local M = 3.0 earthquake occurred afterwards near Bad Fischau on 11 December 2013 in a hypocentral distance of 14.7 km with distinct PGV of 1152 µm/s.

The second short and tiny normal dip-slip movement by 0.004 mm was registered on 6 August 2014 about two months after a local M = 2.7 earthquake near Bad Fischau on 8 June 2014 in a hypocentral distance of 8.6 km and with PGV of 1427 µm/s.

The third undistinguished phase comprised subhorizontal downward compression by 0.005 mm on 24 November 2015. This fault activity happened about one month after a distinct local M = 2.5 earthquake on 26 October 2015 in Breitenau in a hypocentral distance of 11.3 km.

4.5. Geierkogel Cave (LA fault system)

The observation period in Geierkogel Cave lasted from 1 July 2014 to 31 August 2016 and 28 displacement events were registered. The total cumulative displacement (*Dc*) within this period was 0.009 mm, while the total sum of all individual displacement events (*Ds*) was 0.165 mm (Table 2). Although the temperature variations (*ΔT*) were mostly less than 0.1 °C (except for one event with 0.3 °C and six events with thermal difference of 0.2 °C), the index of periodicity was relatively low (*Ip* = 0.05) (Table 1). The average annual rate of the cumulative displacement was 0.005 mm/year. The cumulative displacement vector had a character of a subhorizontal upward transtensional sinistral movement of the hanging block with the orientation of 005/−06°.

Five remarkable activity phases were observed in course of the observation (Fig. 14). The first undistinguished one on 18 August 2014 comprised only tiny dextral movement with counter clockwise rotation (Fig. 14). A M = 1.1 earthquake occurred about two weeks later on 2 September in about 7.5 km hypocentral distance to SW (Figs. 8 and 14).

The distinct second phase started as a sudden clockwise vertical rotation and tiny subvertical upward dilation on 10 December 2014, followed by downward movement and further continuous counter clockwise vertical blocks rotation until beginning of February 2015, when the kinematic behaviour changed. On 2 and 17 February,

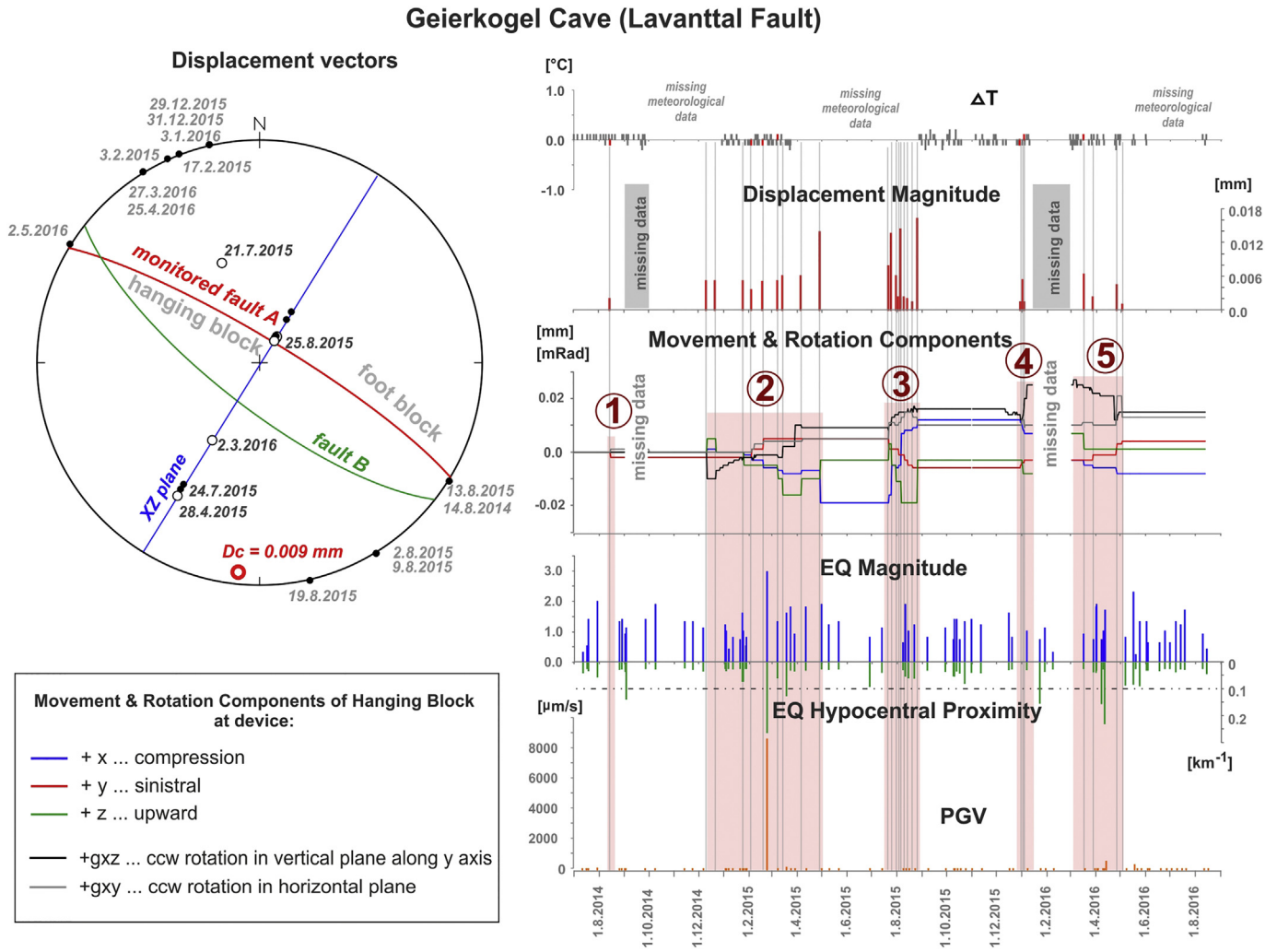

Fig. 14. Review of the fault activity in Geierkogel Cave (Lavanttal Fault) within the period from 1 July 2014 to 31 August 2016. For details see captions of Fig. 10. Remarkable displacements over 0.01 mm are labelled in black, smaller displacements less than 0.01 mm but surely not caused by thermal variations are labelled in grey.

respectively, the fault blocks moved as transtensional sinistral strike-slip with dilation component and rotated horizontally counter clockwise (Fig. 14). Five days later after the second sinistral strike-slip at this dextral fault, a distinct M = 3 earthquake occurred on 22 February 2015 near Judenburg with a focal depth of 3 km and the epicentral distance only 2.4 km to the West. A couple of days after this earthquake, the hanging block moved downwards and rotated vertically counter clockwise, while in April it moved again as a subhorizontal upward dilation. The whole fault activity period was accompanied by several other local earthquakes (Fig. 14).

The third activity phase in summer 2015 was manifested by relatively big displacements. It started as a tiny subvertical upward dilation by 0.008 mm on 21 July 2015 followed by a downward compression with continuous dextral component and continuous counter clockwise horizontal and vertical rotations. It terminated by a distinct reverse fault slip by 0.016 mm on 25 August 2015. A group of earthquakes occurred during a second half of this phase in hypocentral distances of 15–30 km that terminated alongside with this period.

The fourth and fifth activity phases from the end of December 2015 to May 2016 were separated by a technical failure and most probably they were one single phase (Fig. 14). It started first as clockwise vertical rotations from mid to end of December, when it turned to continuous counter clockwise vertical rotations, tiny transtensional sinistral dilations on 29 and 31 December, subvertical downward dilation on 1 January and again tiny transtensional sinistral dilations on 3 January 2016. About 20 days later two very weak earthquakes occurred on 23 January at LA, situated in a hypocentral distance of 7 and 8 km, respectively.

After the technical failure, the fault activity was manifested by upward dilation by 0.018 mm on 2 March 2016, continuous clockwise block vertical rotation, tiny transtensional sinistral dilations from the end of March to end of April, and a sinistral strike slip on 2 May 2016 (Fig. 14). The local seismicity comprised two very near earthquakes on 8 April (M = 0.7) and 12 April 2016 (M = 1.7) in a hypocentral distance of 6.6 and 4.4 km, respectively, and another shallow M = 0.8 earthquake on 7 May in the Fohnsdorf Basin in a hypocentral distance of 12.1 km (Figs. 8 and 14).

4.6. Obir Cave (PAL fault system)

Within the observation period in Obir Cave from 1 July 2014 to 31 August 2016, 55 fault displacement events were registered. The total cumulative displacement (*Dc*) was 0.095 mm and revealed almost dip-slip oriented 159/22° (dip direction/dip angle) of the south-eastern (hanging) block. The total sum of all individual displacement events (*Ds*), on the other hand, was 0.295 mm (Table 2). The temperature variations (*ΔT*) were greatest in winter reaching up to 1.7 °C, while the summer seasons were relatively thermally stable (Fig. 13). The Index of

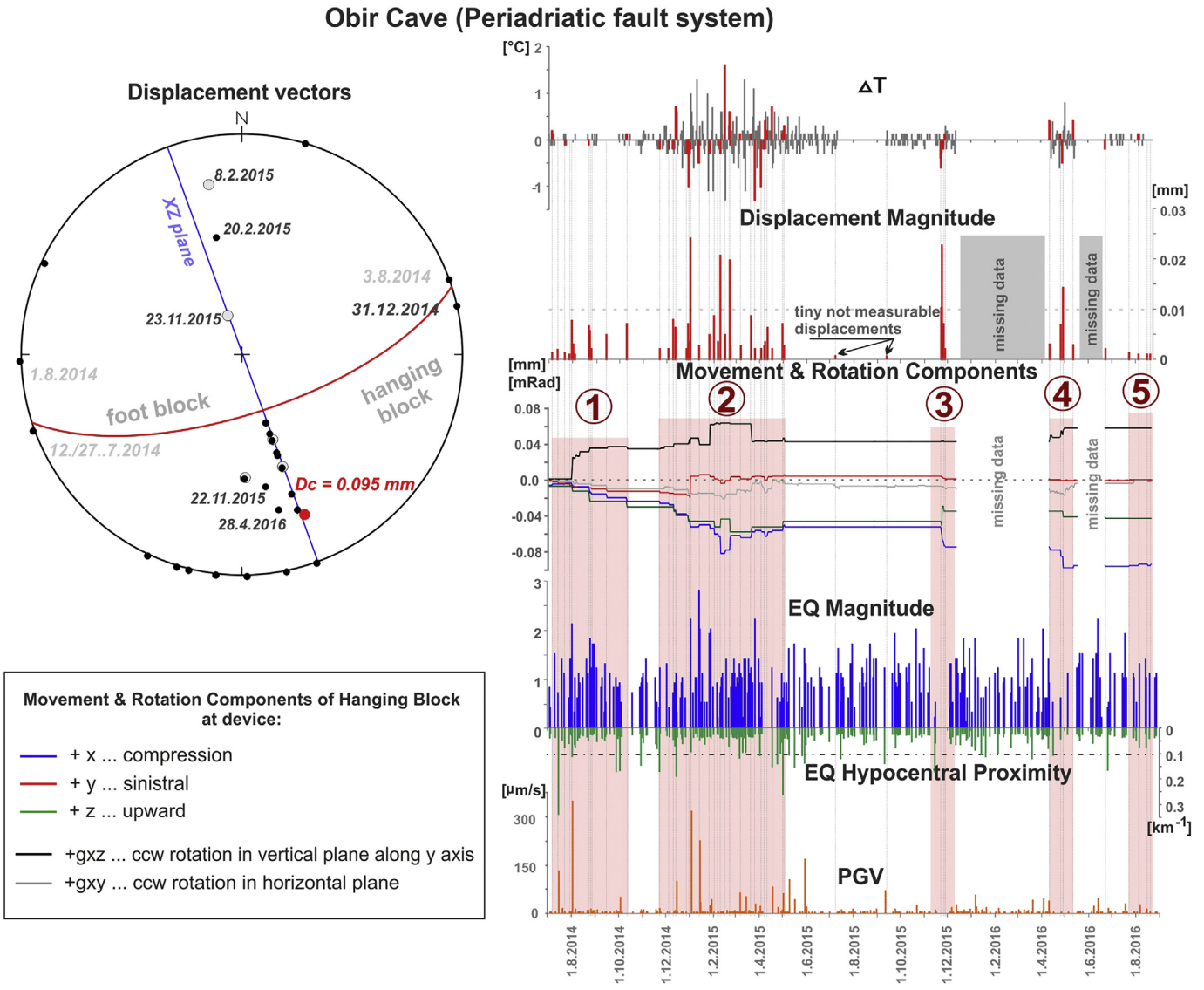

Fig. 15. Review of the fault activity in Obir Cave (Obir Fault adjacent to the Periadriatic Fault) within the period from 1 July 2014 to 31 August 2016. For details see captions of Fig. 10. Remarkable displacements over 0.01 mm are labelled in black, smaller displacements below 0.01 mm but surely not affected by thermal variations are labelled in grey.

periodicity for the presented period was relatively low (*Ip* = 0.32) indicating the rather reversible nature of the displacements. The average annual rate of the cumulative displacement was 0.052 mm/year.

In most of the cases, the hanging block displacement was normal dip-slip parallel with some dilational component, and dextral transtensional dilation (Fig. 15 left). Other displacements were i.e.: sinistral as well as dextral strike slip, fault compression and hanging block subhorizontal downward compression and upward dilation (Fig. 15).

Five remarkable activity phases were observed during the observation (Fig. 15). The first one was registered already in summer 2014 (Fig. 15). It started with a tiny dextral strike-slip on 12 and 27 July, transtensional dextral dilation on 1 August, that changed to sinistral strike-slip on 3 August, but was accompanied by continuous and decelerating counter clockwise vertical rotations. This activity phase was then terminated by a tiny dip slip normal movement on 8 October. It was accompanied by relatively higher local seismicity as well (Fig. 15). The most remarkable M = 2.1 earthquake with strong PGV effect occurred immediately after the dextral strike slips on 2 August in a hypocentral distance of 9.3 km situated directly on the Obir fault (Figs. 8D and 15). Shortly after this earthquake, the fault displacement switched to the sinistral mode on 3 August.

The second distinct phase started on 21 November and 3 December 2014 by tiny dextral transtensional dilations, followed by a variety of tiny normal dip-slip and transtensional movements. At the beginning of this phase, weak M = 0.4 and two M = 1.1 earthquakes occurred on 23 November and 15 December, respectively (Fig. 8D). The most remarkable displacement occurred on 31 December as a sinistral strike slip by 0.024 mm (Fig. 15), after which the fault activity changed again to tiny variable dextral and sinistral trends. Three days after the distinct sinistral strike-slip on 31 December, a remarkable M = 2.2 earthquake occurred directly within the PAL core zone about 5 km to the South at a hypocentral distance of 11.2 km on 3 January 2015. Another M = 2.8 earthquake with distinct PGV values followed on 14 January about 32 km to SSE in Slovenia on the other side of the PAL transpressional zone. Two distinct subhorizontal movements occurred later in February, which comprised upward fault dilation by 0.021 mm on 8 February and downward fault compression by 0.020 mm on 20 February 2015 (Fig. 15), followed by three nearby earthquakes, i.e. M = 1.3 on 7 March, M = 0.2 on 11 March, and M = 1.4 on 15 March (Fig. 8D). Three tiny subvertical upward compressions on 20 March, 30 April and 6 May terminated this fault activity period. Local seismic activity quieted about a month later as well.

In summer 2015, only two very tiny and unquantifiable displacements at the resolution limit and horizontal rotations were recorded on 5 July and 12 September. They occurred at very similar time as two nearby very weak earthquakes on 16 July and 11 September in 8.6 and 7.4 km hypocentral distance. The displacements were manifested only by subtle change in the Moiré pattern of the TM71 device.

The third distinct fault activity phase occurred in autumn 2015 and started on 22 November 2015 as a normal faulting with dilation component by 0.010 mm, changed to subvertical upward dilation by 0.023 mm on 23 November, and followed by tiny normal faulting and dilations until 27 November. This phase followed a weak very near M = 0.2 earthquake that occurred in a hypocentral distance of 6 km on 15 November (Figs. 8D and 15). Unfortunately, we do not have any information on the further fault activity as the device was seriously damaged by a lightning stroke. Soon after repair in April 2016, the fault revealed activity again. This fourth phase, comprising tiny dilations, one compression and a distinct dip-slip normal movement by 0.014 mm on 28 April, occurred shortly after local M = 1.4 and M = 0.2 earthquakes on 10 and 15 April, respectively. After this period the device failed again due to enormous air humidity. In July/August 2016, only some tiny displacements occurred during the last registered undistinguished fifth phase (Fig. 15).

5. Interpretation and discussion

Despite its relatively short duration (up-to 2.5 years), high-resolution three dimensional direct monitoring of subsidiary faults and their master faults revealed distinct activity patterns thanks to the relatively high seismotectonic activity in the Eastern Alps over the period 2013–2016. The study benefited from the application of one of the first automated reading prototypes of the high-resolution 3D extensometers TM71 designed at the Institute of Rock Structure and Mechanics in Prague available since 2009–2013. Previous data readings had been performed manually using a photo-sensitive paper and flash. Automated reading units enabled us to (i) significantly increase the data-reading frequency over much longer periods and (ii) to take into account even the smallest movements close to the resolution limit, thereby avoiding the negative effects of manual manipulation with the devices. Unfortunately, the challenging wet cave environment with high CO_2 concentrations caused some technical failures and damage of electronic parts during observation.

5.1. Ambiental effect

We considered the possible influence of air and rock temperature variations on the measured data producing apparent fault movements. Thermal variations mostly affect the X axis of the TM71 device causing apparent fault compressions (when the arms heated) and dilations (when cooled down). As approved by other authors, the thermal influence diminishes rapidly with depth (Gosar et al., 2009) and the seasonal length variation amplitude decreases from around 1 mm at the ground surface to less than 0.05 mm at depths of more than 10 m (Briestenský et al., 2010), depending on the cave microclimate. In climatically stable caves the thermal variations could be even less. We tried to eliminate this effect by (i) situating the monitoring sites into shielded caves with relatively stable climate, (ii) continuously measuring cave-air temperature and (iii) measuring the fault activity over at least a full annual climatic season.

We used the *index of periodicity* to identify the thermal influence and to better understand the periodic and reversible versus the irreversible nature of the recorded displacements within a given period. In the caves adjacent to the SEMP fault system (Emmerberg and Bullen Cave), as well as in Eisenstein Cave (VBT fault), the index of periodicity was relatively high in accordance to a relatively stable cave climate with the thermal variations being less than 1 °C between single measurements. The dynamic cave climate of Zederhaus Cave (MM fault) was, on the other hand, characterized by a low index of periodicity and indicated by a statistically evident alignment of most of the records along the X axis. These displacements were not described in detail. Similar low *IP* index was registered in Obir Cave (PAL fault system). Whereas in Geierkogel Cave adjacent to the LA fault this index was very low despite a relatively stable cave climate. Here we suppose that it was associated with variable longer trends of faulting within a broader fault zone. The variable fault behavior is probably controlled by the interplay of endogenous effects and gravitational-mass relaxation, block rotations and by hydrogeological and other processes.

5.2. Constraints of the minimum displacements at resolution limit

The fault activities observed at our monitored sites were often on the resolution limit of the device and some of the tiny displacements were aligned along the horizontal (XY) plane or along the XZ plane of the TM71 device. This was the result of an undetected movement component being below the resolution limit. Therefore, such small displacements of about 1–5 μm were only carefully considered as they could be disoriented.

5.3. Fault activity

Our study evidenced that the monitored subsidiary faults (i) revealed macroscopic geological markers of recent strain and (ii) are still continuously active at a micrometer level. The displacements were usually clustered in remarkable activity phases. The faults revealed a variety of horizontal and vertical block rotations, displacement magnitudes and vector orientations depending on the geological setting but varied also in time at each individual site even within a particular activity phase. This is similar to the monitored Californian faults, where a significant fraction of the total slip is typically accommodated by fault creep that can be continuous or episodic, and that varies throughout the earthquake cycle and from one fault to another (Wei et al., 2013).

Due to the relatively short observation period and several technical failures, it is difficult to evaluate precisely, whether the phases over the Eastern Alps were synchronized or not. However, some inconspicuous indications of a regional fault activity pattern over the whole mountain chain are possible (Fig. 16).

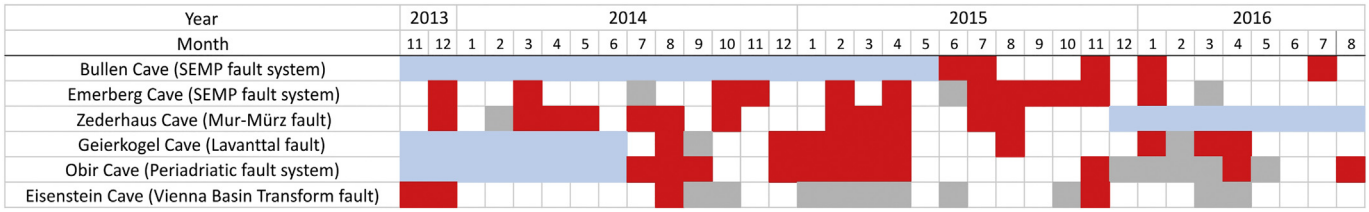

Fig. 16. Schematic chart presenting fault activity phases over the Eastern Alps in 2013–2016: white – fault dormant, red – fault active, light blue – device not installed, grey – device failure. (For interpretation of the references to colour in this figure legend, the reader is referred to the web version of this article.)

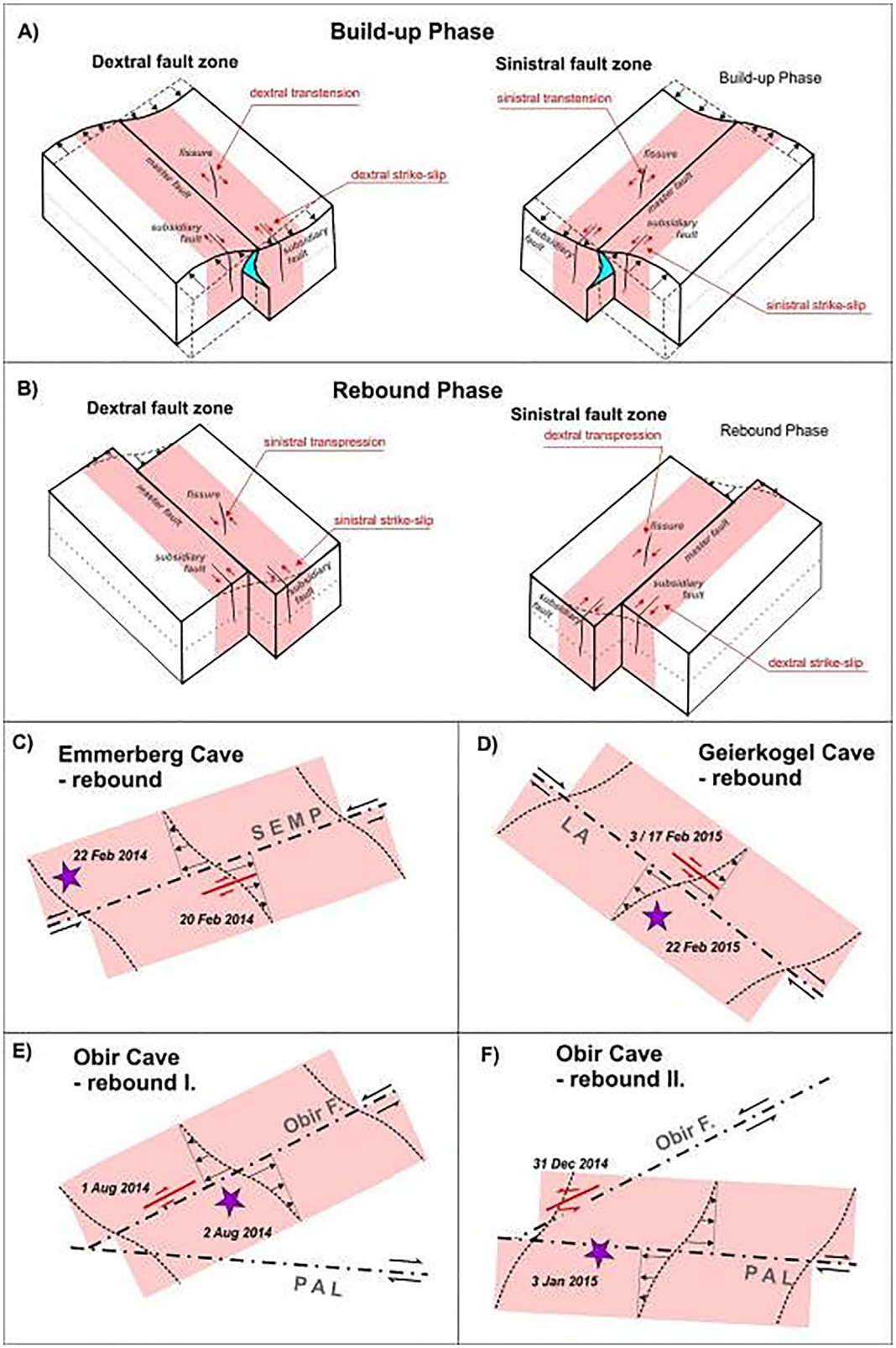

Fig. 17. Subsidiary fault displacements in context of the elastic rebound theory: (A) regions on either sides of a dextral (left) and sinistral (right) strike-slip fault locked by friction are in steady motion, each respective side of the fault is being strained elastically and elastic strain is accumulated over the interseismic period. Subsidiary faults and fissures are reactivated and reveal identical displacements like the general faulting pattern; (B) in the rebound phase the elastic strain overcomes the fault strength, the strained band along the activated fault rebounds back and the respective fault walls get into their new positions. As the deformation during rebound is biggest in the core zone near the master fault and decreases towards the particular blocks, discontinuities such as subsidiary faults reveal due to the deformation asymmetry countervailing displacement. This was documented by the events (C) at SEMP fault in Emmerberg Cave on 20 February 2014, (D) at LA fault in Geierkogel Cave on 3 and 17 February, and at PAL fault system in Obir Cave (E) on 1 August 2014 and (F) 31 December 2014. Purple stars indicate epicentres of particular distinct earthquakes, block diagrams in (A) and (B) after USGS (2018). (For interpretation of the references to colour in this figure legend, the reader is referred to the web version of this article.)

5.4. General trends

Besides the individual displacement events, the total cumulative vectors of displacement characterize the overall trends over the entire observation period. This parameter reduced the reversible movements and, despite the rather short observation period, it can be an indicator comparable to the overall geological setting of each particular locality. The two sites at the SEMP fault system showed quite diverse patterns. The NNW-SSE striking fault located near the SEMP fault system's central part in Bullen Cave had a final cumulative displacement by 0.062 mm along the vector 097/−45°. Although this is somehow an unexpected result for this area, similar upward dilation of the fault was observed also macroscopically at a nearby place in the cave. This vector has a similar orientation as had the macroscopic vector of the reverse active fault in the southern part of the cave. This could be the first direct evidence of present-day reverse faulting in the area of the Totes Gebirge Mts. The easternmost termination of SEMP fault (Emmerberg Cave) on the other hand, revealed much less activity during a much longer observation period and the total cumulative displacement was only 0.040 mm along 209°/31° with an oblique transtensional dextral component.

The total cumulative displacement vector at the fault associated to the Vienna Basin Transfer Fault in Eisenstein Cave of 0.051 mm was represented only by five particular displacement events throughout the observation period. The eastern (hanging) block moved approximately by 0.026 mm/year along a vector 106/61° in accordance with the regional active-tectonic pattern and the observed crevice character of the cave indicating eastward opening and subsidence towards the Vienna Basin.

The Mur-Mürz Fault in Zederhaus Cave with the highest activity so far and the biggest cumulative displacement by 0.351 mm revealed an order of magnitude higher than at the other sites. The high annual fault-slip rate of 0.191 mm/year corresponds to high local seismicity, which is the highest one in the Eastern part of the Eastern Alps (Lenhardt, 1995). In addition, the cumulative displacement vector orientation 288/29° was similar to the overall documented sinistral strike-slip kinematics of the master Mur-Mürz Fault (Linzer et al., 2002).

Surprisingly, in Geierkogel Cave (Pöls-Lavanttal fault system) the total cumulative displacement was relatively low by only 0.009 mm in a transtensional sinistral mode along 005/−06° despite its stable climate.

Total cumulative displacement along the Obir fault adjacent to the PAL fault system by 0.095 mm was almost dip-slip normally oriented along 159/22°. The normal-faulting character of the movement and topographic indications such as pressure ridges along the slope foot and fault-associated series of scarps on the mountain ridge near the monitored site suggest that the movement along the fault was dominantly caused by gravitational mass movement and that tectonic effects played only a minor role in the total displacement.

Compared to the GNSS long-term monitoring of the Eastern Alps by Grenerczy (2005), Bus et al. (2009), or Serpelloni et al. (2016), our observed annual average displacement rates calculated from the total cumulative values along the particular faults are about one or two orders of magnitude smaller. As our measurements are taken selectively at particular subsidiary faults not covering the entire fault systems, our annual displacement rates of much smaller values seem to be plausible and realistic in comparison to GNSS data.

5.5. Interplay with local seismicity

The particular displacements were aseismic. The aseismic slow slip is expected to be a common process in the Eastern Alps as the deformation in the Alps occurs in a more ductile manner compared to, e.g. the Himalayas (Dal Zilio et al., 2018). On the other hand, the fault activity phases usually occurred simultaneously with periods of higher local seismicity, but in locally seismically quiet periods the faults were mostly dormant. Khoshmanesh and Shirzaei (2018) explained similar behaviour at San Andreas Fault: while creeping segments are suggested to act as seismic rupture barriers, slow-slip events on these zones might promote seismicity on adjacent locked segments.

We found a specific pattern in Eisenstein Cave at the margin of the Vienna Basin in a transtensional tectonic regime. The fracture usually became active showing sporadic displacements with a 1–2 months' delay after a locally prominent nearby earthquake within the Vienna Basin. This was probably the result of a specific energy accumulation and dissipation mechanism at gravitationally controlled normal faults described by Doglioni et al. (2015). It seems that the transtension within the VTB core zone increased the gravitational potential at the margin, but the accumulated elastic energy was released aseismically with the delay.

5.6. Countervailing displacements

The monitored subsidiary strike-slip faults sometimes revealed displacements completely opposite to the general kinematics of their master faults. These enigmatic events usually occurred a couple of days prior to distinct local earthquakes. We explain these countervailing displacements by the elastic rebound theory (Fig. 17), which was first postulated by Reid (1910) for the San Andreas Fault. As the regions on either side of a fault, which is locked by friction (Fig. 17A), are in steady motion, each respective side of the fault is being strained elastically (Scholz, 2002). Locally significant discontinuities such as active subsidiary faults and fissures are reactivated as they enhance translating the elastic strain into a brittle mode. The elastic strain within the deformation band is accumulated over the interseismic period until the moment, when it overcomes the fault strength. The strained bands along the activated fault rebound back and the respective fault walls get into their new positions (Fig. 17B). During the accumulation phase, the discontinuities within the strained band reveal identical displacements as the general faulting pattern (Fig. 17A). During the rebound phase the strained rock adjacent to the master fault is displaced relatively more than rock towards the blocks' interior, and therefore the subsidiary faults reveal the countervailing displacement (Fig. 17B). This is documented by the events on 20 February 2014 at SEMP fault in Emmerberg Cave (Fig. 17C), on 3 and 17 February at LA fault in Geierkogel Cave (Fig. 17D), and on 1 August 2014 and 31 December 2014 at the PAL fault system in Obir Cave (Fig. 16E and F).

Although our observation period was relatively short and thus we do not have a good statistical sample, it seems that the “countervailing events” within the elastic deformation band could be an indicator of an impending nearby earthquake within the rebound zone. We suppose that detecting such anomalous countervailing events in real-time could substantially contribute to an effective early warning, which until now has been impossible in case of earthquakes.

6. Conclusions

The study summarizes the present-day kinematic behaviour of active faults attributed to the major fault systems of the extruding Eastern Alps over a 1.5–2.5-year period between 2013 and 2016. The frequency, magnitudes, and vectors of the particular hanging-walls' aseismic displacements at particular faults showed a variety of values and faulting regimes within several activity phases that usually also coincided with periods of higher local seismicity.

The biggest activity and average annual displacement rates were observed in the seismically most active regions along the Mur-Mürz fault, along the Periadriatic fault and in the North of the SEMP central part in Totes Gebirge Mts. However, the annual displacement rates were mostly about one order of magnitude smaller than the rates of the entire crustal wedges revealed from GNSS.

The fault dilations and compressions were mostly associated with thermal-volumetric variations, but displacements oriented identically to the master-fault or with an upward component were attributed to

tectonic creep and strain built-up during the interseismic period. On the other hand, the countervailing displacements opposite to the master fault kinematics were most probably caused by elastic rebound. They were usually registered a few days in advance to distinct local earthquakes that were simultaneously activated at locked segments within the same deformation band. Therefore, the countervailing events could be an indicator of an impending nearby earthquake within the rebound zone and their better understanding and real-time detecting could be a step forward to an effective earthquake early warning in similar geological settings.

Acknowledgements

This study was conducted in the framework of the project P25884-N29 "Active tectonics and recent dynamics of micro-displacements along major fault systems of the Eastern Alps registered in caves (SPELEOTECT)" financed by the Austrian Science Fund (FWF) and was done in close collaboration with the Institute of Rock Structure and Mechanics of the Czech Academy of Sciences. The TM71 raw data were processed by Monika Hladká and Jana Šreinová from the Institute of Rock Structure and Mechanics, supported by the longterm conceptual development research organisation of the Institute of Rock Structure & Mechanics RVO: 67985891. We are grateful to Peter Baumgartner, Jan Blahůt, Karl Filz, Zdeněk Fučík, Karl Kolb, Norbert Kucher, Andreas Langer, Christopher Langer, Harald Langer, Franz Moitzi, Tomáš Nýdl, Pauline Oberender, Christa Pfarr, Johann Georg Pollerus, Martin Schmölz, Robert Seebacher, Jakub Stemberk, Hans Stieg, Christian Varch, and especially to Gerhard and Renate Winkler for their great support and help at the monitoring sites. Ewald Brückl, Kurt Decker, Helmut Hausmann, Wolfgang Lenhardt, Xavi Martí, Rudolf Pavuza and Matt Rowberry provided helpful advices, discussions, and feedback. The authors are thankful to the governments of Lower Austria, Styria, Carinthia and Upper Austria for providing high-resolution digital terrain models and to local authorities of Bad Eisenkappel, Judenburg, Bad Fischau, and Spittal am Semmering, and Forest Administrations of Emmerberg and Tauplitz for allowing us to install the monitoring devices within their properties. Christa Pfarr revised the language, and Philippe Agard and two anonymous reviewers are acknowledged for their effort and help in improving the overall manuscript quality.

References

Agnew, D.C., 2007. Before PBO: an overview of continuous strain and tilt measurements in the United States. J. Geodetic Soc. Jpn. 53, 157–182.

Baroň, I., Plan, L., Grasemann, B., Mitrovic, I., Lenhardt, W., Hausmann, H., Stemberk, J., 2016. Can deep seated gravitational slope deformations be activated by regional tectonic strain: first insights from displacement measurements in caves from the Eastern Alps. Geomorphology 259, 81–89. https://doi.org/10.1016/j.geomorph.2016.02.007.

Basili, et al., 2013. SHARE – The European Database of Seismogenic Faults. – Online Database. http://diss.rm.ingv.it/share-edsf/sharedata/SHARE_WP3.2_Map.html.

Beidinger, A., Decker, K., 2011. 3D geometry and kinematics of the Lassee flower structure: implications for segmentation and seismotectonics of the Vienna Basin strike-slip fault, Austria. Tectonophysics 499 (1–4), 22–40.

Beidinger, A., Decker, K., Roch, K.H., 2011. The Lassee segment of the Vienna Basin fault system as a potential source of the earthquake of Carnuntum in the fourth century a.d. Int. J. Earth Sci. 100 (6), 1315–1329. https://doi.org/10.1007/s00531-010-0546-x.

Blahůt, J., Baroň, I., Sokol, L., Meletlidis, S., Klimeš, J., Rowberry, M., Melichar, R., García-Cañada, L., Martí, X., 2018. Large landslide stress states calculated during extreme climatic and tectonic events on El Hierro, Canary Islands. Landslides 15 (9), 1801–1814. https://doi.org/10.1007/s10346-018-0993-1.

Briestenský, M., Košťák, B., Stemberk, J., Petro, L., Vozár, J., Fojtíková, L., 2010. Active tectonic fault microdisplacement analyses: a comparison of results from surface and underground monitoring in western Slovakia. Acta Geodyn. Geomater. 7, 387–397.

Briestenský, M., Rowberry, M.D., Stemberk, J., Stefanov, P., Vozár, J., Šebela, S., Petro, L., Bella, P., Gaal, L., Ormukov, C., 2015. Evidence of a plate-wide tectonic pressure pulse provided by extensometric monitoring in the Balkan Mountains (Bulgaria). Geol. Carpath. 66 (5), 427–438. https://doi.org/10.1515/geoca-2015-0035.

Briestenský, M., Hochmuth, Z., Litva, J., Hók, J., Dobrovič, R., Stemberk, J., Petro, L´., Bella, P., 2018. Present-day stress orientation and tectonic pulses registered in the caves of the Slovenský kras Mts. (South-Eastern Slovakia). Acta Geodyn. Geomater. 15 (2), 93–103. https://doi.org/10.13168/AGG.2018.0007. (190).

Brückl, E., Behm, M., Decker, K., Grad, M., Guterch, A., Keller, G.R., Thybo, H., 2010. Crustal structure and active tectonics in the Eastern Alps. Tectonics 29, TC2011. https://doi.org/10.1029/2009TC002491. (17 pp).

Bus, Z., Grenerczy, G., Tóth, L., Mónus, P., 2009. Active crustal deformation in two seismogenic zones of the Pannonian region: GPS versus seismological observations. Tectonophysics 474, 343–352. https://doi.org/10.1016/j.tecto.2009.02.045.

Cello, G., Kostak, B., 2003. Active faults: analysis, processes and monitoring. J. Geodyn. 36 (1–2), 1–340.

Dal Zilio, L., van Dinther, Y., Gerya, T.V., Pranger, C.C., 2018. Seismic behaviour of mountain belts controlled by plate convergence rate. Earth Planet. Sci. Lett. 482 (2018), 81–92. https://doi.org/10.1016/j.epsl.2017.10.053.

Decker, K., 1996. Miocene tectonics at the Alpine Carpathian junction and the evolution of the Vienna basin. Mitteilungen der Gesellschaft der Geologie- und Bergbaustudenten in Österreich 51, 33–44.

Decker, K., Peresson, H., 1996. Tertiary kinematics in the Alpine-Carpathian-Pannonian system: links between thrusting, transform faulting and crustal extension. In: Wessely, G., Liebl, W. (Eds.), Oil and Gas in Alpidic Thrustbelts and Basins of Central and Eastern Europe. 5. EAGE, pp. 69–77 Spec. Publ.

Decker, K., Peresson, H., Faupl, P., 1994. Die miozäne Tektonik der östlichen Kalkalpen: Kinematik, Paläospannungen und Deformationsaufteilung während der “lateralen Extrusion” der Zentralalpen. In: Jahrbuch der Geologischen Bundesanstalt. 137. pp. 5–18 Nr. 1, S.

Decker, K., Peresson, H., Hinsch, R., 2005. Active tectonics and Quaternary basin formation along the Vienna Basin Transfer fault. Quat. Sci. Rev. 24 (3–4), 307–322.

Doglioni, C., Carminati, E., Petricca, P., Riguzzi, F., 2015. Normal fault earthquakes or graviquakes. Sci. Rep. 5, 12110. https://doi.org/10.1038/srep12110.

Elliott, J.R., Walters, R.J., Wright, T.J., 2016. The Role of Space-based Observation in Understanding and Responding to Active Tectonics and Earthquakes. https://doi.org/10.1038/ncomms13844.

Fodor, L., Jelen, B., Márton, E., Skaberne, D., Čar, J., Vrabec, M., 1998. Miocene-Pliocene tectonic evolution of the Slovenian Periadriatic fault: implications for Alpine-Carpathian extrusion models. Tectonics 17 (5), 690–709.

Frisch, W., 1979. Tectonic progradation and plate tectonic evolution of the Alps. Tectonophysics 60, 121–139.

Frisch, W., Dunkl, I., Kuhlemann, J., 2000. Post-collisional orogen-parallel large-scale extension in the Eastern Alps. Tectonophysics 327 (3–4), 239–265.

Fügenschuh, B., Seward, D., Mancktelow, N., 1997. Exhumation in a convergent orogen: the western Tauern window. Terra Nova 9, 213–217.

Georgieva, V., Melnick, D., Schildgen, T., Ehlers, T.A., Lagabrielle, Y., Enkelmann, E., Strecker, M.R., 2016. Tectonic control on rock uplift, exhumation, and topography above an oceanic ridge collision: Southern Patagonian Andes (47°S), Chile. Tectonics 35 (6), 1317–1341. https://doi.org/10.1002/2016TC004120.

Gosar, A., Šebela, S., Kostak, B., Stemberk, J., 2009. Surface versus underground measurements of active tectonic displacements detected with TM71 extensometers in western Slovenia. Acta Carsol. 38, 213–226.

Grenerczy, G., 2005. Tectonic implications of the GPS velocity field in the northern Adriatic region. Geophys. Res. Lett. 32, L16311. https://doi.org/10.1029/2005GL022947.

Grenerczy, G., Kenyeres, A., 2006. Crustal deformation between Adria and the European platform from space geodesy. In: Pinter, N. (Ed.), The Adria Microplate: GPS Geodesy, Tectonics and Hazards. NATO Sci. Ser. IV, vol. 61. Springer, Dordrecht, Netherlands, pp. 321–334. https://doi.org/10.1007/1-4020-4235-3_22.

Handy, M.R., Ustaszewski, K., Kissling, E., 2015. Reconstructing the Alps–Carpathians–Dinarides as a key to understanding switches in subduction polarity, slab gaps and surface motion (Review article). Int. J. Earth Sci. (Geol. Rundsch.) 104 (1), 1–26. https://doi.org/10.1007/s00531-014-1060-3.

Hardebeck, J., Michael, A., 2006. Damped regional-scale stress inversions: methodology and examples for southern California and the Coalinga aftershock sequence. J. Geophys. Res. Solid Earth 111, B11310. https://doi.org/10.1029/2005JB004144.

Hardege, J., 2018. Hydrotectonics of the Eisensteinhöhle (MS. Master's Diploma Thesis). University of Vienna (58 pp).

He, M., Wang, Y., Tao, Z., 2010. A new early-warning prediction system for monitoring shear force of fault plane in the active fault. J. Rock Mech. Geotech. Eng. 2 (3), 223–231. https://doi.org/10.3724/SP.J.1235.2010.00223.

Hintersberger, E., Decker, K., Lomax, J., Lüthgens, C., 2018. Implications from palaeoseismological investigations at the Markgrafneusiedl Fault (Vienna Basin, Austria) for seismic hazard assessment. Nat. Hazards Earth Syst. Sci. 18 (2), 531–553. https://doi.org/10.5194/nhess-18-531-2018.

Hölzel, M., Decker, K., Zámolyi, A., Strauss, P., Wagreich, M., 2010. Lower Miocene structural evolution of the central Vienna Basin (Austria). Mar. Pet. Geol. 27 (3), 666–681.

Isacs, B., Molnar, P., 1971. Distribution of stresses in the descending litosphere from a global survey of focal-mechanism solutions of mantle earthquakes. Rev. Geophys. Space Phys. 9 (1), 103–174.

Ishii, H., Yamauchi, T., Matsumoto, S., Hirata, Y., Nakao, S., 2002. Instrument for earthquake prediction study: some observed examples of precursory and co-seismic phenomena relating to earthquake swarms and application of the instrument for rock mechanics. In: Ogasawara, H., Yanagidani, T., Ando, M. (Eds.), Seismogenic Processes Monitoring. Taylor & Francis (426 pp).

Khoshmanesh, M., Shirzaei, M., 2018. Episodic creep events on the San Andreas Fault caused by pore pressure variations. Nat. Geosci. 11, 610–614.

Klimeš, J., Rowberry, M., Blahut, J., Briestenský, M., Hartvich, F., Košťák, B., Rybář, J., Stemberk, J., Štěpančíková, P., 2012. The monitoring of slow-moving landslides and assessment of stabilisation measures using an optical–mechanical crack gauge. Landslides 9 (3), 407–415.

Košťák, B., 1991. Combined indicator using moiré technique. In: Sorum, G. (Ed.), Field

Measurements in Geomechanics. A.A. Balkema, Rotterdam, pp. 53–60.
Košťák, B., Avramova-Tačeva, E., 1988. A method for contemporary displacement measurement on a tectonic fault. J. Geodyn. 10, 115–125.
Košťák, B., Popp, K., 1966. Moiré strain gauges. Strain 2, 1–12.
Košťák, B., Nikonov, A.A., Pereděrin, V.L., Sidorin, A.J., Enman, S.V., 1992. Monitoring of microdisplacements along ruptures at the Garm Geodynamic Test Site. Izvestiya Phys. Solid Earth 28, 761–775.
Košťák, B., Mrlina, J., Stemberk, J., Chán, B., 2011. Tectonic movements monitored in the Bohemian Massif. J. Geodyn. 52 (2011), 34–44.
Kurz, W., Wölfler, A., Rabitsch, R., Genser, J., 2011. Polyphase movement on the Lavanttal Fault Zone (Eastern Alps): reconciling the evidence from different geochronological indicators. Swiss J. Geosci. 104, 323–343.
Lenhardt, W.A., 1995. Regional earthquake hazard in Austria. In: Duma (Ed.), Proceedings of the 10th European Conference on Earthquake Engineering, Balkema, Rotterdam, (63–68 pp).
Linzer, H.-G., Decker, K., Persson, H., Dell'Mour, R., Frisch, W., 2002. Balancing lateral orogenic float of the Eastern Alps. Tectonophysics 354, 211–237.
Marti, X., Rowberry, M.D., Blahůt, J., 2013. A MATLAB code for counting the moiré interference fringes recorded by the optical-mechanical crack gauge TM71. Comput. Geosci. 52, 164–167. https://doi.org/10.1016/j.cageo.2012.09.029.
McCalpin, J., 1996. Paleoseismology, 1st edition. Academic Press, pp. 588.
Neubauer, F., Genser, J., Handler, R., 2000. The Eastern Alps: result of a two-stage collision process. Mitt. Österr. Geol. Ges. 92 (1999), 117–134.
Parcharidis, I., Kokkalas, S., Fountoulis, I., Foumelis, M., 2009. Detection and monitoring of active faults in urban environments: time series interferometry on the cities of Patras and Pyrgos (Peloponnese, Greece). Remote Sens. 2009 (1), 676–696. https://doi.org/10.3390/rs1040676.
Peresson, H., Decker, K., 1997. Far-field effects of Late Miocene subduction in the Eastern Carpathians: E-W compression and inversion of structures in the Alpine-Carpathian-Pannonian region. Tectonics 16 (1), 38–56.
Pinel-Puysségur, B., Grandin, R., Bollinger, L., Baudry, C., 2014. Multifaulting in a tectonic syntaxis revealed by InSAR: the case of the Ziarat earthquake sequence (Pakistan). J. Geophys. Res. Solid Earth 119, 1–17. https://doi.org/10.1002/2013JB010564.
Plan, L., Hartmann, W., Winkler, G., 1996. Speleological map of Eisenstein Cave. MS.. Archive of the Speleologic Association of Vienna and Lower Austria, Vienna.
Plan, L., Spötl, C., Pavuza, R., Dublyansky, Y., 2009. Hypogene Caves in Austria—Hypogene Speleogenesis and Karst Hydrogeology of Artesian Basins. 1. Ukrainian Institute of Speleology and Karstology, pp. 121–128 Special Paper.
Plan, L., Grasemann, B., Spötl, C., Decker, K., Boch, R., Kramers, J., 2010. Neotectonic extrusion of the Eastern Alps: constraints from U/Th dating of tectonically damaged speleothems. Geology 38 (6), 483–486. https://doi.org/10.1130/G30854.1.
Poltnig, W., Herlec, U., 2012. Full geological description of Geopark Karavanke. Geopark Karawanken/Karavanke Authority(207 pp (Available online)).
Ratschbacher, L., Frisch, W., Linzer, H.G., Merle, O., 1991. Lateral extrusion in the Eastern Alps, part 2: structural analysis. Tectonics 10/2, 257–271. https://doi.org/10.1029/90TC02623.
Reid, H.F., 1910. The mechanics of the earthquake, the California earthquake of April 18, 1906. In: Report of the State Investigation Commission. Vol. 2 Carnegie Institution of Washington, Washington, D.C.
Reinecker, J., Lenhardt, W.A., 1999. Present-day stress field and deformation in eastern Austria. Int. J. Earth Sci. 88, 532–550.
Rinaldi-Montes, N., Rowberry, M., Frontera, C., Garcés, J., Baroň, I., Blahůt, J., Pérez-López, R., Pennos, C., Martí, X., 2017. A contactless positioning system for monitoring discontinuities in three dimensions with geological and geotechnical applications. Rev. Sci. Instrum. 88, 074501. https://doi.org/10.1063/1.4993925.
Roux, P., Ben-Zion, Y., 2013. Monitoring fault zone environments with correlations of earthquake waveforms. Geophys. J. Int. 196 (2), 1073–1081.
Rowberry, M.D., Kriegner, D., Holý, V., Frontera, C., Llull, M., Olejník, K., Martí, X., 2016. The instrumental resolution of a moire extensometer in light of its recent automatisation. Measurement 91 (2016), 258–265. https://doi.org/10.1016/j.measurement.2016.05.048.
Sachsenhofer, R.F., Kogler, A., Polesny, H., Strauss, P., Wagreich, M., 2000. The Neogene Fohnsdorf Basin: Basin formation and basin inversion during the lateral extrusion in the Eastern Alps (Austria). Int. J. Earth Sci. 89, 415–430.
Salcher, B.C., Meurers, B., Smit, J., Decker, K., Hölzel, M., Wagreich, M., 2012. Strike-slip tectonics and Quaternary basin formation along the Vienna Basin fault system inferred from Bouguer gravity derivatives. Tectonics 31, TC3004. https://doi.org/10.1029/2011TC002979.
Salomon, M.L., Grasemann, B., Plan, L., Gier, S., Schöpfer, M.P.J., 2018. Seismically-triggered soft-sediment deformation structures close to a major strike-slip fault system in the Eastern Alps (Hirlatz cave, Austria). J. Struct. Geol. 110, 102–115.
Schmid, S.M., Fügenschuh, B., Kissling, E., Schuster, R., 2004. Tectonic map and overall architecture of the Alpine orogeny. Eclogae Geol. Helv. 97 (1), 93–117. https://doi.org/10.1007/s00015-004-1113-x.
Schmied, A., Schmied, M., 1975. Speleological Map of Zederhaus Cave, Spittal am Semmerring. MS.. Archive of the Speleologic Association of Vienna and Lower Austria, Vienna (1 pp).
Scholz, C.H., 2002. The Mechanics of Earthquakes and Faulting, 2nd edition. Cambridge University Press978-0-521-65540-8 471 pp.
Schönlaub, H.P., Schuster, R., 2015. Die Zweiteilung der Karawanken und ihre erdgeschichtliche Entwicklung, Geol. Bundesanst. Wien. 978-3-85316-080-0.
Schuster, R., Daurer, A., Krenmayr, H.G., Linner, M., Mandl, G., Pestal, G., Reitner, J., 2014. Rocky Austria. Geological Survey of Austria, Vienna (80 pp).
Šebela, S., Vaupotič, J., Stemberk, J., Košťák, B., 2010. Direct measurement of present-day tectonic movement and associated radon flux in Postojna Cave, Slovenia. J. Cave Karst Stud. 72 (1), 21–34 (ISSN 1090-6924).
Seebacher, R., 2014. Speleological map of Bullen Cave. MS. Archive of the Speleological Club for Upper Austria, Bad Mitterndorf.
Serpelloni, E., Vannucci, G., Anderlini, L., Bennett, R.A., 2016. Kinematics, seismotectonics and seismic potential of the eastern sector of the European Alps from GPS and seismic deformation data. Tectonophysics 688, 157–181. https://doi.org/10.1016/j.tecto.2016.09.026.
Sokol, L., Melichar, R., Baroň, I., 2018. Present-day stress inversion from a single near-surface fault: a novel mathematical approach. J. Struct. Geol. 117 (2018), 163–167. https://doi.org/10.1016/j.jsg.2018.09.013.
Solar, E., Trimmel, H., Thaler, H., 1970. Speleological Map of Wartburggrotte, Obir Cave. MS. Archive of the Speleologic Association of Vienna and Lower Austria, Vienna (1 pp).
Spelix Online GIS Database of Autrian Caves. https://www.spelix.at.
Spötl, C., Fairchild, I.J., Tooth, A.F., 2005. Cave air control on dripwater geochemistry, Obir Caves (Austria): implications for speleothem deposition in dynamically ventilated caves. Geochim. Cosmochim. Acta 69 (10), 2451–2468. https://doi.org/10.1016/j.gca.2004.12.009.
Stein, S., Liu, M., Camelbeeck, T., Merino, M., Landgraf, A., Hintersberger, E., Kübler, S., 2015. Challenges in assessing seismic hazard in intraplate Europe. Geol. Soc. 432 (4 November 2015), 13–28. https://doi.org/10.1144/SP432.7. London, Special Publications.
Stemberk, J., Košťák, B., 2007. 3-D trend of aseismic creep along active faults in western part of the Gulf of Corinth, Greece. Acta Geodyn. Geomater. 4 (1), 53–65 (Praha).
Stemberk, J., Košťák, B., Vilímek, V., 2003. 3D monitoring of active tectonic structures. J. Geodyn. 36 (1–2), 103–112 (ISSN 0264-3707).
Stemberk, J., Hartvich, F., Blahůt, J., Rybář, J., Krejčí, O., 2017. Tectonic strain changes affecting the development of deep seated gravitational slope deformations in the Bohemian Massif and Outer Western Carpathians. Geomorphology 289, 3–17.
Süssenbeck, H., Komenda, G., Maurer, J., Süssenbeck, M., 1971. Speleological map of Emmerberghöhle (Burghöhle) bei Winzendorf (Fischauer Vorberge). MS. Archive of the Speleological Association of Vienna and Lower Austria, Vienna (1 pp).
Tamburini, A., Del Conte, S., Ferretti, A., Cespa, S., 2014. Advanced satellite InSAR technology for fault analysis and tectonic setting assessment. Application to reservoir management and monitoring. International Petroleum Technology Conference, 19-22 January, Doha, Qatarhttps://doi.org/10.2523/IPTC-17574-MS. (9 pp).
Umnig, E., Weber, R., 2017. Aktive Tektonik entlang der Mur-Mürz-Störung und im Wiener Becken (MS). Bericht für Schools & Quakes-Abschlussbericht (BMWFW), pp. 25–30.
USGS, 2018. Earthquake Processes and Effects. Earthquake Hazard Program Website. https://earthquake.usgs.gov/research/eqproc/grdmotion.php.
von Czoernig-Czernhausen, W., 1924. Speleological Map of Geierkogel Cave. MS. Archive of the Speleologic Association of Vienna and Lower Austria, Vienna (1 pp).
Vrabec, M., Pavlovčič, Prešeren P., Stopar, B., 2006. GPS study (1996–2002) of active deformation along the Periadriatic fault system in northeastern Slovenia: tectonic model. Geol. Carpath. 57 (1), 57–65.
Wei, M., Kaneko, Y., Liu, Y., McGuire, J.J., 2013. Episodic fault creep events in California controlled by shallow frictional heterogeneity. Nat. Geosci. 6, 566–570.
Weissl, M., Hintersberger, E., Lomax, J., Lüthgens, C., Decker, K., 2017. Active tectonics and geomorphology of the Gaenserndorf Terrace in the Central Vienna Basin (Austria). Quat. Int. 451, 209–222. https://doi.org/10.1016/j.quaint.2016.11.022.
Wölfler, A., Kurz, W., Fritz, H., Stüwe, K., 2011. Lateral extrusion in the Eastern Alps revisited: refining the model by thermochronological, sedimentary, and seismic data. Tectonics 30, TC4006. https://doi.org/10.1029/2010TC002782. (15 pp).